

On the He II Emission In η Carinae and the Origin of Its Spectroscopic Events¹

John C. Martin²

K. Davidson²

Roberta M. Humphreys²

D. J. Hillier³

K. Ishibashi⁴

ABSTRACT

We report Hubble Space Telescope (HST) observations of emission in η Carinae near 4680 Å, presumably He II λ 4687, which are not spatially resolved from the central star. The emission was not detected in the spectrum from 1998.0 to 2003.0, or after the spectroscopic event in 2003.5. It appeared in early 2003, rapidly grew to a larger brightness than the previous authors reported, and then disappeared suddenly near 2003.5. For several weeks the λ 4687 luminosity was too high to explain easily in most proposed models for η Car's spectroscopic events. According to our analyses, this feature appears most consistent with a wind-disturbance or mass-ejection type of model with relatively high gas densities. An unusual form of radiative excitation, making use of trapped He II λ 304 resonance photons, may have played a major role.

Subject headings: binaries: general, line: profiles, stars: individual (η Carinae), stars: variables: other, stars: winds, outflows

¹This research is part of the Hubble Space Telescope Treasury Project for Eta Carinae, supported by grants GO-9420 and GO-9973 from the Space Telescope Science Institute (STScI), which is operated by the Association of Universities for Research in Astronomy, Inc., under NASA contract NAS 5-26555.

²School of Physics and Astronomy, University of Minnesota, 116 Church Street SE, Minneapolis, MN 55455; martin@etacar.umn.edu

³Department of Physics and Astronomy, University of Pittsburgh, 3941 O'Hara Street, Pittsburgh, PA 15260

⁴Center for Space Research, Massachusetts Institute of Technology, 77 Massachusetts Avenue, NE80-6011, Cambridge, MA 02139

1. Introduction

Steiner & Damineli (2004) reported the detection of He II $\lambda 4687$ emission⁵ in ground-based spectra of η Carinae. This feature represents a far higher excitation or ionization state than other lines seen in this object under normal conditions. Thus it may be a valuable clue to the mechanism behind η Carinae’s 5.5-year cycle and to the structure of the shock fronts that produce X-rays in the stellar wind (see refs. cited below). Here we report observations of the same feature with higher spatial resolution and other advantages using the Space Telescope Imaging Spectrograph (HST/STIS). Essentially, we find:

- Broad emission was present between 4680Å and 4685Å during the mid-2003 spectroscopic event.
- The emission is not spatially resolved from the central star.
- However, the HST data contradict certain crucial details reported by Steiner & Damineli.
- The explanation which those authors offer for the He II emission is not adequate to explain the energy budget. The feature is far more surprising and enigmatic than they indicated.

Qualitatively, one expects shock fronts near Eta Carinae to produce weak He II emission; but quantitatively *the observed flux presents a difficult energy-supply puzzle*. Either the deduced intrinsic strength is in error for reasons unknown, or some extraordinary process occurred during the 2003 spectroscopic event.

So far as we know, Gaviola (1953) reported the earliest suspected detection of He II $\lambda 4687$ in this object. He listed two separate emission features near 4680Å and 4686Å that were comparable in strength to He I $\lambda 4714$. According to the notes in his paper, each of them appeared only in one observation during the interval from April 1944 through March 1951. Gaviola obtained data during a spectroscopic event in 1948, but understandably he did not recognize it as such and his notes do not state whether that was the time when the emission in question appeared. If he observed emission at 4686Å on one occasion in 1948 and then 4680Å somewhat later, the wavelength shift would resemble that which occurred in 2003 (see below). Unfortunately the published record does not state whether this was the case and it is possible that Gaviola’s spectra showing this emission feature did not correspond to a “spectroscopic event” (see below).

⁵In this paper we consistently quote vacuum wavelengths.

Thackeray (1953) reported that a weak feature occurred near 4687 Å at some time between April 1951 and June 1952. Feast (2004, *private communication*), re-examining Thackeray’s plates, confirms that such emission may have been present on June 14, 1951 and July 10, 1951. In itself this evidence is weak, since Thackeray and Feast both expressed skepticism and the observations did not coincide with an “event.” However, we note that 1951-2 was an unusual period in η Car’s recovery from its great eruption. Indeed, the photometric and spectroscopic record from 1941 to 1953 suggests that the stellar wind was in transition from one state to another. The high excitation emission lines appeared for the first time in Gaviola’s spectra beginning in 1944. Prior to that time they were not seen (Feast et al. 2001; Humphreys & Koppelman 2005). The star also brightened considerably during this time (O’Connell 1956) and de Vaucouleurs & Eggen (1952) observed a uniquely abrupt increase in brightness in March 1952 which coincided with the start of the current long-term brightening trend; see Martin (2005) and Davidson et al. (2005a), and refs. cited therein. Therefore one should not dismiss the possibility that Thackeray’s plates really did show He II λ 4687.

Since the 1950’s Eta Car has undergone periodic spectroscopic events which are characterized by the disappearance of high excitation lines that normally dominate its ground-based spectra. These events occur regularly every 5.5 years (Damineli 1996; Whitelock et al. 1994). The most recent one occurred in late June 2003. Preceding a spectroscopic event, the X-ray flux rises, becomes increasingly unstable or chaotic, and then “crashes” to near zero flux (Ishibashi et al. 1999; Corcoran 2005). The most common explanation for the X-ray light curve is a colliding wind binary model (Pittard & Corcoran 2002) where the secondary star and the shock emitting region are eclipsed by the higher wind densities flowing out from the poles of the primary star (referred to in this paper as the “eclipse model”). But there is still no realistic orbit based on Doppler velocities (Davidson et al. 2000) or spectroscopic evidence for the proposed companion. The data presented here demonstrate that the periodic shell ejection model (Zanella et al. 1984), with or without an undetected companion to trigger it, is a more viable model because it has not been ruled out by any observations and is able to explain the 4680 Å emission with fewer complications.

The Hubble Treasury Project for η Carinae was intended primarily to observe the mid-2003 spectroscopic event, so we obtained STIS data frequently throughout 2003. In this paper we discuss the 4680Å emission feature seen in those data and its evolution since 1998. We report HST/STIS data but we also refer to ground-based VLT/ESO data (Stahl et al. 2005) obtained during the same interval. Often we refer to the feature in question as “4680Å,” its approximate wavelength at its maximum strength in the STIS data, because it is quite broad and in principle the He II λ 4687 identification has not been fully confirmed. (See Appendix A for details.) We also present a theoretical assessment of the energy budget

implied by the line’s strength, which appears almost paradoxical.

The three most crucial points on which we disagree with Steiner & Damineli (2004) are the following:

- The brief maximum of the 4680Å feature was more extreme than they supposed, because at the time of its maximum the emission appears to have been dominated by a broad underlying component which filled in the spectrum between two strong bracketing emission features.
- Those authors reported that an emission feature is *usually* present near 4687 Å with an equivalent width in the range 50–200 mÅ, see their Figure 2. However, during 1998.0–2003.0 and after 2003.5 the HST/STIS data showed no feature at those levels within about 200–300 AU of the star. The lack of this alleged weak feature is important because Steiner & Damineli based a “velocity curve” on it (their Figure 3).
- They proposed a fairly specific explanation for the He II emission. A quantitative analysis, however, shows that it is inadequate; indeed one can use the data to argue against, rather than for, the type of spectroscopic event that they advocate for η Car. The observed emission is not easy to explain.

Details regarding these points will be explained throughout this paper.

2. STIS CCD Data

The spectra in this paper were obtained as part of the η Carinae HST Treasury Project (Davidson 2004a) and were reduced using non-standard methods which are too complex to describe briefly here. Information regarding these techniques and the Treasury Project can be found online at <http://etacar.umn.edu> and will be described in detail in a series of forthcoming papers. Each one-dimensional spectrum discussed in this paper is essentially a 0.1" x 0.25" spatial sample: the pixel size is about 0.05", the slit width is about 2 CCD columns, each spectral extraction sampled 5 CCD rows, and the spectral resolution is roughly 40 km/s at 4680Å. We applied an aperture correction to the absolute flux which was calculated using an observation of the spectrophotometric standard Feige 110 with the same slit and extraction parameters. The STIS resolves the central star from nearby bright ejecta which heavily contaminate ground-based spectra of η Carinae. Therefore, the spectra of the central star presented in this paper are unlike ground-based observations in that we specifically exclude material outside $r \approx 200 - 300$ AU. Note that when we refer to “the

star” or “ η Carinae,” we mean the central object and its wind, not the bright ejecta and Homunculus nebula. If the star is double then it is unresolved by the HST.

In most of our analyses and figures we do not average adjacent pixels or smooth the STIS/CCD spectra. The signal-to-noise of the reduced data is on the order of 100 to 180 for a sample width of 0.3Å (see Table 1 and Appendix B). We have resisted combining pixels to improve the signal since that operation implicitly smooths the spectrum and can deceptively alter its noise characteristics.

Our measurements confirm that the 4680Å feature spatially coincides with the central star, as previously remarked by Gull (2005). To the accuracy of our measurements, the emission has the same cross-dispersed profile as the continuum. Therefore, the source of this emission is unresolved from the central star on a scale of $\pm 0.02''$ or about 45 – 50 AU. The emission feature is found only in the spectrum of the central star and does not originate in the ejecta, although we list a few caveats in Appendix C.

The most likely identification of the 4680Å feature is He II $\lambda 4687.0$ but strictly speaking this identification has not been confirmed. For various reasons we have not been able to detect any other He II lines in the spectrum (see Appendix A for details). Since He II $\lambda 4687.0$ is observationally and theoretically the most sensible identification, we have proceeded on this assumption at many points in the following sections.

3. The Flux and Equivalent Width of the Feature

Figure 1 illustrates that the level of the underlying continuum can be a significant source of systematic error. Relatively strong emission features bracket 4680Å on either side: Fe II around 4660Å to the blue and He I $\lambda 4714$ to the red. Those features make it difficult to set the continuum level over that interval when the 4680Å emission becomes strong and fills the trough between them. We measured the continuum flux in an interval devoid of features between 4742.5Å and 4746.5Å. Note that there is no significant difference between the continuum measured at 4744Å and 4605Å. Therefore, this method closely approximates the average spectral flux around 4687Å when the feature in question is not present, i.e. at most times (lower horizontal dotted line in Figure 1).

The continuum-subtracted fluxes and equivalent widths of the 4680Å feature and continuum between 4675.0Å and 4694.0Å are given in Table 1. The limits of integration intentionally omit a small part of the wings of the feature in order to exclude He I $\lambda 4714$ P-Cygni absorption and [Fe III] $\lambda 4702$ which vary around the time of the spectroscopic event. As a result, some of our measurements may somewhat underestimate the flux in the 4680Å fea-

ture. The quoted errors are one sigma uncertainties which include contributions from both photon statistics and detector noise. However, they do not include systematic errors which may have been introduced through contamination by other spectral features or in our approximation of the underlying continuum. For details about how the errors were calculated see Appendix B.

For the reasons stated above, the largest equivalent width we measured (2.4Å on MJD 52813.8) is much larger than one would have found if the continuum were estimated using only the wavelength range 4650Å to 4700Å (Figure 1). Therefore it considerably exceeds the maximum quoted by Steiner & Damineli. The wavelength interval filled by the feature between 4670Å and 4693Å was smooth and well behaved in all of our STIS data except from April to June 2003 (Figure 2).

4. Temporal Evolution

The first significant detection of the 4680Å feature in the STIS data was on MJD 52683.1 (2003 February 12), about 140 days before the mid-2003 event. It then increased in strength until it reached a strong maximum on MJD 52813.8 (2003 June 22), near the time of the event. During the period of growth its profile undulated significantly (Figure 2). On MJD 52791.7 (2003 June 1), the emission appeared to be centered within a few hundred km s^{-1} of the rest wavelength for He II $\lambda 4687$ with a gently sloping blue tail. Generally, however, most of the emission was several hundred km s^{-1} blueward of 4687Å with a gently sloping red tail. Steiner & Damineli (2004) report similar activity in their observations with better temporal sampling. This dramatic velocity shift may explain why Gaviola (1953) reported two separate emission features, if they appeared in two distinct observations (see Section 1 above).

The feature increased in strength over the course of about six months, then it abruptly disappeared. It is completely absent on MJD 52825.4 (2003 July 5), only twelve days after its maximum in the STIS data, and is not detectable in any of the subsequent STIS observations through the last one obtained on MJD 53071.2 (2004 March 6, Figure 3). The small positive and negative values of the “line flux” before MJD 52683.1 and after MJD 52813.8 (Table 1) are mostly due to changes in the wing of the Fe II complex at 4660Å which creeps in on the blue side of the integration limits (see Figure 1). We are reassured in this explanation by the fact that those small fluctuations closely mirror the general behavior of the broad component of the Fe II features in the spectrum.

The VLT/UVES spectra reported by Stahl et al. (2005) reveal an interesting wrinkle

regarding the disappearance of this line. Due to the geometry of the Homunculus nebula, the light reflected at certain points gives a view from different latitudes above the central star’s surface (Smith et al. 2003). One such location, referred to in the literature as FOS4, gives a pole-on view of the central star with a light-time delay of about 20 days relative to our view of the central star directly along the line of sight (Meaburn et al. 1987). Stahl et al. (2005) show that the disappearance of 4680Å as seen from FOS4 is not only earlier (when corrected for the light travel time) but probably also a more gradual process than when viewed from lower latitudes. However, this is difficult to gauge due to the sparse temporal sampling of the VLT/UVES data. Note that in the context of the eclipse model (Pittard & Corcoran 2002) it is fortuitous that the feature would disappear at nearly the same time at FOS4 and along our direct line of sight. A simple comparison with the STIS data (which is disadvantaged by even more sparse temporal sampling) hints that there certainly are differences in the phenomenon which depend on the viewing angle (Figure 4). These differences should be studied in more detail and must be explained by any serious theoretical models.

Steiner & Damineli (2004) state that the 4680 Å emission line maintained an equivalent width on the order of 100 mÅ throughout most of the spectroscopic cycle. This assertion is particularly important because they derived a “velocity curve” from the weak feature (their Fig. 3). However, this is *not* supported by the STIS spectra (see Appendix B for a detailed discussion) or the VLT/UVES data (Stahl et al. 2005). Our observations before MJD 52683.1 and after MJD 52813.8 all appear very similar to MJD 52825.4 (Figures 2 and 3). As previously demonstrated, the flux between 4675Å and 4695Å at those times is consistent with the continuum flux measured in a clean part of spectrum between 4742.5Å and 4746.5Å (Figure 1). Therefore, we conclude that no emission in this feature is present in our observations before MJD 52683.1 and after MJD 52813.8, at a level of 40 mÅ. Steiner & Damineli may have detected emission from some extended source, even though we detect none in close proximity to the star. We give a detailed discussion of the spatial extent of the emission region in Appendix C. The reappearance of the feature in their data 10 to 20 days after the peak may be light reflected by the surrounding ejecta, delayed by light travel time, but we cannot judge this possibility without knowing the length and orientation of their slit. Moreover, the fact that the VLT/UVES spectra do not show the feature reflected in the ejecta outside the time of the event also challenges their interpretation. In any case if the 4680Å feature was not observed on the central star then their velocity curve is questionable⁶.

The gradual growth and abrupt disappearance of the 4680Å feature also correlates with other observed changes in the central star of Eta Carinae around the 2003.5 spectroscopic

⁶Unfortunately their paper does not include tracings of the feature when it was weak or details of their observations and error analysis.

event (Figure 5). The initial appearance of the feature on MJD 52683.1 corresponds to the appearance of P-Cygni absorption in Balmer H α (Davidson et al. 2005a). The simultaneous appearance and growth of these features is not unexpected if they are both produced in the stellar wind or winds.

As the 4680Å feature grew, so did the H α P-Cygni absorption and the near-infrared brightness (Whitelock et al. 2004). The time of maximum 4680Å flux in the STIS data (MJD 52813.8) was only about one day before the abrupt decline in near-infrared brightness (J, H and K magnitudes). This synchronized behavior is almost certainly more than coincidental. It implies a close association between the 4680Å emission feature and the mechanism which is responsible for the sharp drop in near-infrared brightness.

The 4680Å maximum occurred well after the peak of the 2–10 keV X-ray brightness (Corcoran 2005)⁷. In fact, nearly every feature in the optical, UV, and near infrared spectrum which varies with the spectroscopic event peaked almost simultaneously, reaching a climax *after* the X-rays had already substantially declined. To be sure, the STIS observation on MJD 52791.7 almost coincided with the hard X-ray peak, so that even if the maximum occurred between observations on MJD 52791.7 and MJD 52813.2, that was after the hard X-rays had begun their decline. Steiner & Damineli (2004) measured the peak 4680Å brightness with better temporal sampling a few days following our observation on MJD 52813.2. On this point we have no disagreement. We disagree, however, concerning the relationship between λ 4687 and the observed 2–10 keV X-ray flux. Examining the data record closely, one may reasonably conclude that these two observables were *anti*-correlated during June of 2003— which is clear in Fig. 5, but not in figures with more compressed timescales.⁸ In the most publicized scenario for η Car’s spectroscopic event, the X-rays disappear because they move behind the primary star’s dense wind (see, e.g., Pittard & Corcoran (2002)). But the timing discrepancy noted above seems different from what one would expect in such a model. We assume, as did Steiner and Damineli, that the He II emission originates near the X-ray shock fronts (see Section 5 below); if so, why did the hard X-rays fade well before

⁷http://lheawww.gsfc.nasa.gov/users/corcoran/eta_car/etacar_rxte_lightcurve/

⁸Various authors have plotted observations of the 2003 event in terms of “phase” in the 5.5-year cycle instead of standard time measurements such as MJD. Phase is potentially misleading because, contrary to what one might assume, it has no unique zero-point. It is set empirically and does not necessarily correlate with a special point in the orbit of the proposed secondary star. The hard X-rays observed with RXTE are particularly ill-suited to define t_0 , because they had strong random fluctuations in both 1997 and 2003, their detailed behavior differed between those two events, and the true shape of their minimum was hidden by detector noise. The near-IR flux suffers from none of these objections (Whitelock et al. 2004) and therefore would be better for defining an empirical t_0 .

the He II emission? One might argue that for about 10 days, intervening gas had begun to block the X-rays but not the visual-wavelength light from the same vicinity. However, one would expect the latter to be reduced by Thomson scattering, particularly with the high local densities that we find necessary for reasons discussed in Section 5 below. Thus a simple eclipse model offers no clear explanation of why the He II emission rose *rapidly* as the 2–10 keV X-rays faded⁹. Moreover, such a model postulates a special orbit orientation in order to make the event occur at the right time – but the VLT data on location FOS4 (see above), representing an entirely different line of sight, showed a He II event at nearly the same time.

At first glance the abrupt disappearance of the $\lambda 4687$ may seem evocative of an eclipse, but closer examination makes this doubtful. In an eclipse model the intervening “object” is thought to be the polar wind of primary star, not the star itself. (Based on the structure of the Homunculus, the orbit inclination is presumably close to 45° .) One does not expect the polar wind to be sharp edged and also the size of the $\lambda 4687$ -emitting region is most likely at least 2 AU. In the observed disappearance time of less than two weeks, however, the secondary star should have moved less than 2 AU. Moreover, the $\lambda 4687$ brightness was increasing rapidly before its peak (Fig. 5). If its subsequent disappearance was caused only by an eclipse, then one must conclude that the intrinsic maximum (i.e., after the eclipse had started) must have been even brighter than we suppose in Section 5 – which increases the difficulty of explaining it. Consider, on the other hand, a wind-disturbance, mass-ejection, or shock-front disintegration model. Several of the processes described in Section 5 are very sensitive to velocity gradients, density, and other parameters; therefore one can easily imagine a rapid intrinsic collapse of the emission rate. Arguments like these are not sufficient to disprove an eclipse model, but they do suggest that alternatives may be better.

In a binary model there is little doubt that each spectroscopic event occurs near the time of periastron; this assertion is based on the rapid onset of the event and no authors have expressed strong disagreement. There are many plausible reasons for an X-ray and spectroscopic event to occur as the companion star approaches periastron (Davidson 1999, 2002, 2005c). But an eclipse model requires additional assumptions, e.g. concerning the orbit orientation we mentioned above. Therefore, in our opinion the simplest hypothesis in the context of the binary model is that periastron (or the approach to it) is itself the chief cause of a spectroscopic event in η Car. Very likely the secondary star does move behind the primary wind afterward – perhaps a few weeks later – but by that time the most interesting phenomena have already occurred. No observations have yet contradicted the idea that if

⁹If the 2–10 keV X-ray decline observed in June 2003 was caused *only* by attenuation, then its intrinsic peak must have been much higher. Obviously, this would make the requirements for hard X-ray production even more extreme.

there is a secondary companion, the event is chiefly associated with periastron passage rather than an eclipse. The He II $\lambda 4687$ emission appears to support this view in two ways:

1. As emphasized above, some process had already eliminated most of the hard X-rays well before the main growth of $\lambda 4687$. (We suspect that copious soft, not hard, X-rays were being produced at the climax of the event. Unfortunately, large column densities obscure them from us.)
2. The maximum $\lambda 4687$ luminosity required a disturbance or enhancement in the primary wind's density (see Section 5).

5. The Energy-budget Problem

5.1. Generalities

He II $\lambda 4687$ emission is normally a recombination line in a He^{++} region, arising in decays from the He^+ $n = 4$ level to $n = 3$. Eta Car, however, cannot produce sufficient He^{++} in the usual way, since contrary to observation the required very hot stellar continuum would also create a bright high-excitation photoionized region in the inner Homunculus nebula. Therefore, as Steiner & Damineli (2004) noted, in this case the He^{++} probably occurs near shock fronts that produce ionizing soft X-ray emission. Here we review the problem; the $\lambda 4687$ brightness seen in late June 2003 turns out to be more difficult to explain than those authors indicated. A mass ejection event or at least a massive inner-wind disturbance may be necessary to make some of the parameters suitable. Where no specific reference is cited here for a parameter, see Davidson & Humphreys (1997) and Hillier et al. (2001) for η Car or Osterbrock (1989) for ionic data.

To put the question in a more definite context, we consider three alternative shock scenarios during one of η Car's spectroscopic events:

1. The shocks may occur at a wind-wind interface in a binary system, as most authors have supposed for the hard X-rays. In this case we can classify several distinct emission zones sketched in Fig. 6. Regions 1 and 2 are undisturbed parts of the two stellar winds. Region 3 contains shocked gas with $T > 10^6$ K. In regions 4 and 5 near each shock surface, helium is photoionized by soft X-ray photons from region 3. Finally, region 6 consists of shocked gas that has cooled below 10^5 K as it flows outward within region 3; densities are very high there because the local pressure is comparable to the nearby ram pressure of each wind. (Depending on several parameters, region 6

may be farther from the star than our sketch indicates.) In reality, each “region” probably consists of numerous unstable corrugations or separated condensations (see, e.g., Pittard & Corcoran (2002) and refs. therein, and remarks in Davidson (2002)), but the our classification of zones seems broadly valid. There is no reason to expect the observed amount of He II $\lambda 4687$ emission in regions 1 or 2; region 3 is too hot for $\lambda 4687$ emission to be efficient (see below); and region 5 has a much smaller density than region 4. Evidently then, regions 4 and 6 harbor the best conditions for producing He II emission.

2. A spectroscopic event of η Car may instead be a stellar mass-ejection phenomenon, possibly including a shock front moving outward from the primary star (Zanella et al. 1984; Davidson 1999, 2005c). In this case the hypothetical companion star might not exist; but, independent of the binary-vs.-single-star question, an ejection event can produce a relatively large temporary energy supply. As we emphasize later, this may be useful for the He II $\lambda 4687$ emission. The term “ejection event” is rather elastic in this context and may refer merely to a disturbance or temporary rearrangement of the wind’s latitude zones (Smith et al. 2003).
3. Conceptually, at least, it is easy to combine ideas (1) and (2) if the companion star triggers an instability near periastron. In particular, a mass ejection or wind disturbance may suddenly increase the local density of the primary wind, regions 1 and 4 in Fig. 6, thereby changing the colliding-wind parameters and probably destabilizing the shocks (Davidson 2002, 2005c). In this connection we must note an important discrepancy that few authors have emphasized. The often-quoted mass-loss rate of η Car, $\sim 10^{-3} M_{\odot} \text{ yr}^{-1}$, would imply a density of the order of $10^{10.5} \text{ ions cm}^{-3}$ at $r = 2.5 \text{ AU}$ in a spherical wind. In the most commonly cited colliding-wind X-ray model, however, Pittard & Corcoran (2002) used a wind density that was smaller by a factor of ten. Smith et al. (2003) later explained that this seems reasonable *in low-latitude zones* of η Car’s non-spherical wind if most of the mass usually flows toward high latitudes. Thus, if a mass ejection or wind disturbance occurs during a spectroscopic event, the low-latitude wind may suddenly change from the low-density case to a higher-density state. Such a development affects the He II $\lambda 4687$ emission rate for reasons given later in this discussion.

Other scenarios may be possible, but these three seem most obvious. In the remainder of this section we present a quantitative assessment of the He II $\lambda 4687$ problem. We find that the observed emission requires either a very large temporary energy supply rate, or a highly unusual enhancement of the $\lambda 4687$ emission efficiency, or both.

As explained in Appendix D, the peak luminosity of $\lambda 4687$ emission observed with STIS appears to have been about 10^{36} ergs s^{-1} or $10^{47.4}$ photons per second. The uncertainty factor is roughly 2, but this is non-Gaussian and an error factor worse than 3 seems unlikely. Anyway, 10^{36} ergs s^{-1} is comparable to η Car's total 2–10 keV X-ray luminosity. But $\lambda 4687$ is just one emission line, which must be accompanied by much brighter emission in less observable parts of the spectrum; so we are confronted by a serious energy-supply problem.

5.2. The Energy Budget for Normal Excitation Processes

Most of the ionic parameters employed here can be found, explicitly or implicitly, in Osterbrock (1989). If He II $\lambda 4687$ is a recombination line, the peak emission luminosity quoted above implies about $10^{48.1}$ recombination events per second, which is only mildly dependent on the assumed temperature and density.¹⁰ In order to estimate the maximum plausible efficiency for conversion of thermal energy to He II $\lambda 4687$ emission, we make the following assumptions.

- Include only helium and hydrogen recombination plus bremsstrahlung, and omit excitation of heavy ions and expansion cooling. This simplification will lead to an overestimate, not an underestimate, of the He II $\lambda 4687$ efficiency.
- The relevant gas is hotter than 50000 K. In reality, lower temperatures may occur if additional processes dominate the cooling; but in that case, the fraction of energy which escapes as He II recombination radiation is greatly reduced.
- The mass fraction of helium is not much larger than 50% (Davidson & Humphreys 1997; Hillier et al. 2001).
- Only photons with energies less than 54.4 eV (the I.P. of He^+) escape from the He^{++} zones; and

¹⁰ Recombination is more efficient than collisional excitation for this emission line. If $T < 60000$ K in the emitting gas, then the collisional excitation rate is hopelessly small by any standard. At temperatures of the order of 10^5 K, collisionally excited $\lambda 4687$ emission can be comparable to the recombination emission only if the $\text{He}^+/\text{He}^{++}$ ratio is orders of magnitude larger than the values allowed by photoionization, with any photon and electron densities that seem reasonable for this problem. At $T > 3 \times 10^5$ K – e.g., in gas that has recently passed through a shock – collisional ionization of He^+ becomes considerably more rapid than collisional excitation of $\lambda 4687$. In that case, $\lambda 4687$ emission carries away an even smaller fraction of the total energy than we estimate for the recombination process at lower temperatures.

- He^+ is ionized mainly by photons between 54.4 and 550 eV. Most X-ray photons above 550 eV either escape, or are converted into photons below 550 eV following absorption by nitrogen and other heavy elements.
- Temporarily neglect the radiative excitation processes discussed in Section 5.3 below.

In these circumstances, we calculate that He II $\lambda 4687$ emission accounts for less than 0.6% of the escaping radiative energy. This result is unsurprising, since $\lambda 4687$ accounts for only about 1% of the total He II recombination emission in a conventional high-excitation nebula. Of course hydrogen recombination and bremsstrahlung must also occur. *Therefore, if the $\lambda 4687$ luminosity estimated above represents helium recombination, it implies an overall energy supply of at least $10^{38.2}$ ergs s^{-1} , or more than $40000 L_\odot$.* If this originates in shocks it is a formidable requirement, exceeding the total kinetic energy flow usually quoted for η Carinae's entire primary wind. According to Corcoran et al. (2004), other observations appear to suggest the same order of magnitude for the soft X-ray luminosity during the 2003 spectroscopic event. Certain processes discussed in Section 5.3 and Appendix E may allow the stellar UV radiation field to contribute, thereby reducing the X-rays required, but these processes need special conditions. Before exploring them, let us review the requirements for a model with less than 0.6% efficiency.

Can the wind of a hot companion star provide most of the relevant energy as Steiner and Damineli assumed? In a standard colliding-wind scenario, its speed must be about 3000 km s^{-1} in order to account for the observed 2–10 keV X-ray spectrum (Corcoran et al. 2001; Viotti et al. 2002; Hamaguchi et al. 2004). A kinetic energy output of $10^{38.2}$ ergs s^{-1} would thus require a mass-loss rate $\sim 10^{-4.3} M_\odot \text{ yr}^{-1}$. But this is surely an underestimate; expansion and escaping X-rays above 2 keV, rather than soft X-rays, should account for most of the post-shock cooling, and part of the wind may escape the main shocks altogether. Therefore, in a model of this type the peak observed $\lambda 4687$ brightness implies a secondary mass-loss rate of more than $10^{-4} M_\odot \text{ yr}^{-1}$. Even if we have overestimated the peak brightness by a factor of 3 or 4, the remaining deduced rate of $\sim 10^{-4.5} M_\odot \text{ yr}^{-1}$ would be extraordinary for a hot massive star. Evidently, then, a theory of this type requires the extremely unusual primary star to have a very unusual companion, without any clear evolutionary or physical reason. Moreover, a secondary star with such a fast and massive wind must be very hot and luminous, and should therefore produce far more ionizing UV photons than the primary does, including photons capable of ionizing He^0 . Although we do not yet have enough data for a formal calculation, one would expect such an object to photoionize the inner parts of the Homunculus nebula, causing hydrogen emission, [Ne III], etc., far brighter than the modest amounts observed there.

The hypothetical fast secondary wind seems unappealing as a soft X-ray source. Since a 3000 km s^{-1} wind produces temperatures of the order of $kT \approx 10 \text{ keV}$ at its shock surface, the resulting X-ray spectrum emphasizes multi-keV photons which are almost useless for ionizing He^+ . Soft X-rays account for a fraction of the total luminosity, and eventually the gas cools to lower temperatures, but altogether this is not an efficient way to make a He^{++} region. Conditions become more favorable if the characteristic pressure – essentially determined by the density of the primary’s wind – is much higher near periastron than most authors have assumed. In that case the shock structure becomes more complex, which favors soft X-rays (Davidson 2002); and the secondary star’s UV continuum may then supplement the energy budget as we discuss in Section 5.3 and Appendix E. But *that is a fundamentally different type of model*; one of the main points of this paper is the need for high densities. Meanwhile the primary star’s slower, denser wind is normally more suitable for producing soft X-rays. Note, also, that the secondary wind is expected to be relatively steady, because no proposed tidal or radiative effects near periastron would appreciably alter it. That fact precludes some useful temporary effects which appear possible in the primary wind (see next paragraph). In summary, based on a combination of factors, the fast secondary wind seems very unlikely to be the principal energy source for the $\lambda 4687$ -emitting gas unless we alter the assumed parameters of the primary wind near periastron.

With velocities in the range 300 to 1000 km s^{-1} , the primary star’s wind produces characteristic shock-front temperatures $kT < 1.4 \text{ keV}$, most likely $200\text{--}400 \text{ eV}$, quite suitable for ionizing He^+ . Steady mass loss at a rate of $10^{-3} M_\odot \text{ yr}^{-1}$ is not adequate for our purpose, but several effects may improve the situation. For instance, there are independent reasons to suspect that a rapidly growing disturbance – perhaps enhanced mass loss – occurs in low-latitude zones of the primary wind during a spectroscopic event (Zanella et al. 1984; Davidson 1999; Smith et al. 2003; Davidson 2005c). The STIS data indicate that roughly $10^{53.5}$ He II $\lambda 4687$ photons were produced during a 60-day interval in 2003, requiring a total input energy of the order of $10^{44.7}$ ergs if we assume an efficiency of 0.3% for producing $\lambda 4687$. This equals the kinetic energy of $10^{-4} M_\odot$ moving at 700 km s^{-1} . A temporary “extra” mass-flow rate of several times $10^{-3} M_\odot \text{ yr}^{-1}$, passing through shock fronts for several weeks, would thus produce the observed amount of $\lambda 4687$ emission. Moreover, if this material moves faster than the normal low-latitude wind speed, a complex structure of unstable shocks would form around the star, not just at the interface with the secondary wind. Regarding the abrupt peak in the $\lambda 4687$ brightness, note that the apparent time scale may be compressed in this type of scenario. If velocities tend to increase during an event, or if an instability in the shocked gas spreads rapidly, then the time interval for conversion to He II emission can be shorter than the time during which the same material was ejected from the star. In other words, a moderate-speed wind ($V < 1000 \text{ km s}^{-1}$) has some capacity

for storing energy which can then be released with suitable time and size scales. Since the hypothetical material moves roughly 0.4 AU per day, the likely size scale is of the order of several AU, comparable to the periastron distance in a binary scenario.

A proper model would require calculations with more quantitative details than we have given here; but the above ideas seem broadly consistent with the nature of η Car, the general appearance of a spectroscopic event, and the requirements for explaining the He II emission. Admittedly the energy supply appears marginal, but certain radiative processes may enhance the $\lambda 4687$ production rate in this type of model. These are sketched in the next subsection and in Appendixes E and F.

5.3. Special Radiative Excitation Processes

Trapped He II $\lambda 304$ resonance photons can increase the population of He^+ ions in the $n = 2$ level. At sufficiently high gas and photon densities, this effect can enhance He II $\lambda 4687$ in two main ways: (1) Ordinary stellar UV photons with $\epsilon > 13.6$ eV can ionize He^+ from level 2, making the He^{++} region more extensive than one would guess based on the soft X-rays alone. In other words, for indirect reasons stellar UV radiation can supplement the soft X-ray ionization of He^+ . (2) Meanwhile, UV photons near 1215 Å can excite He^+ from the $n = 2$ level to $n = 4$, the upper level for $\lambda 4687$ emission. We discuss this complicated set of problems in Appendixes E and F.

The essential result is that $\lambda 4687$ emission can be substantially enhanced – possibly by a factor of order 10 – in a region where the electron and ion densities exceed $10^{10.2} \text{ cm}^{-3}$. Therefore a model with temporary high densities, as we advocated above, is made easier. The observed rapid growth of the feature just before its peak seems to make sense in this case, because the amplification factor is quite sensitive to the gas density. However, the same effects do not provide sufficient amplification at densities below 10^{10} cm^{-3} . Therefore they seem unlikely to account for $\lambda 4687$ in the lower-density type of colliding wind model proposed by Pittard & Corcoran (2002).

Conceivably the He II $\lambda 4687$ might be excited by stellar photons near 1215 Å, absorbed by He^+ ions in the $n = 2$ level. According to a brief assessment sketched in Appendix G, this phenomenon may account for an equivalent width of the order of 0.1 Å but not much more – so it, too, appears to be inadequate in a low-density model.

Unfortunately these quantitative results depend too strongly on the geometrical assumptions for us to feel entirely confident about them. Most likely we have *overestimated* the enhancement factor, because local inhomogeneities and velocity gradients would allow

$\lambda 304$ photons to escape more easily. (This is especially true in “region 6” of Fig. 6.) On the other hand, since the basic parameters are poorly established, an inventive theorist may be able to construct a low-density model by carefully tailoring the assumptions. Obviously this problem needs more work, including realistic simulations with the appropriate radiative processes and gas-dynamical instabilities. Pending such efforts, the relatively high-density wind disturbance type of model appears to present fewer difficulties than a lower-density colliding wind model that relies largely on eclipse phenomena.

6. Summary

We confirm that an emission feature arose near 4680 \AA just before the mid-2003 spectroscopic event, and that it occurred close to the central star rather than in the diffuse ejecta. Far more interesting, however, are the details that differ from those reported by Steiner & Damineli (2004). Taken in combination, these differences fundamentally alter the theoretical picture.

1. He II $\lambda 4687$ is the obvious and presumably most likely identification for the observed feature. However, we must acknowledge that no other He II feature has been detected to confirm it. Therefore, some other identification may conceivably be correct, although we take it to be He II in the remaining points below.
2. The peak luminosity of the feature appears to have been substantially larger than Steiner & Damineli (2004) reported. As noted in Section 3 above, this depends on the adopted continuum level, which is shown best by the HST/STIS observations.
3. The relationship between the 2–10 keV X-ray flux and $\lambda 4687$ is complex. The apparent X-ray flux peaked significantly earlier, and had already fallen to less than 20% of its maximum at the time when the $\lambda 4687$ flux, the near-IR brightness, and the H α P Cyg absorption reached their maxima together (Fig. 5). In other words, during the last two weeks of June 2003 the $\lambda 4687$ brightness rapidly *rose* while the apparent X-ray flux rapidly *declined*. Although this fact does not necessarily disprove a simple eclipse model for the X-ray behavior, it significantly increases the complexity of such a model.¹¹ On the other hand, the time delay seems consistent with a disintegrated-shock model (Davidson 2002), a mass ejection, and/or a major wind disturbance. In

¹¹With reference to the X-ray eclipse scenario, M. Corcoran has pointed out (priv. comm.) that the true X-ray luminosity maximum may have occurred later than the apparent maximum. However, then one must explain why the $\lambda 4687$ emission was not also reduced at the same time; Thomson scattering should have had

these cases one expects the unstable shock fronts to be producing mainly soft X-rays at the climax of the spectroscopic event – independent of the binary-vs.-single-star question.

4. The $\lambda 4687$ brightness grew at an impressive rate before maximum, but its subsequent abrupt disappearance was even more remarkable. It is not easy to design a sufficiently rapid eclipse model, considering that both the source region and the eclipsing wind are extended.
5. The feature was not detectably present in STIS or VLT/UVES spectra from early 1998 to early 2003, and abruptly disappeared at 2003.5. As explained in Appendix B, no feature with the characteristics reported by Steiner & Damineli was detected in our data outside the build-up to the spectroscopic event. This raises questions about the “velocity curve” shown in their Figure 3.
6. The observed He II $\lambda 4687$ flux requires an overall energy source which is surprisingly large for shocks in the stellar wind or winds. *This is a serious problem.* The model favored by Steiner & Damineli (2004) cannot supply the energy budget needed unless special processes occur (point 7 below) and in that case the observed emission does not directly indicate the secondary star parameters. We suggest that a mass-ejection event might provide enough energy, but detailed models are clearly needed.
7. Radiative excitation processes may contribute to the observed emission (Section 5.3). Our analysis in Appendix E indicates that this may work in a high density model under optimal conditions. The usually quoted eclipse model (Pittard & Corcoran 2002), however, assumed much *lower* densities.
8. The average Doppler velocity (roughly -400 km s^{-1}) and the line width (400 to 1000 km s^{-1}) must also be explained by any acceptable model. The overall velocity dispersion is not very surprising in any of the scenarios mentioned above. The negative average Doppler velocity at maximum, however, seem more consistent with a mass-ejection event than with most of the colliding-wind scenarios that have been proposed. Can there be an alternative configuration?

Pending further developments, the high-density case, e.g., a mass ejection or wind-disturbance scenario, appears the most promising. A lower-density model requires extra

some effect. Such an explanation is made difficult by the fact that the apparent $\lambda 4687$ brightness increased *by a considerable factor* after the apparent X-ray maximum, see Fig. 5.

effort either to provide a sufficient X-ray energy supply, or to make the $\lambda 304$ entrapment processes work (Section 5 above). Thus, in our opinion the main implication of the He II $\lambda 4687$ emission is almost opposite to what Steiner & Damineli (2004) concluded. They interpreted this feature to be an indirect confirmation of the eclipsing binary model.¹² By quantitative analyses we find that the peak $\lambda 4687$ brightness appears to require either a basic revision of the colliding-wind parameters, or, more likely, an enhanced wind density during the spectroscopic event. As emphasized by Davidson (2005c), these competing ideas have fundamentally different implications for the physics of η Car. If a spectroscopic event represents an eclipse or occultation, then it tells us little about the nature of the primary star. A mass ejection or wind disturbance model on the other hand requires some undiagnosed surface instability which must depend on the star’s structure. For an ordinary object one hesitates to invoke an “undiagnosed instability”; but during the past 200 years η Car has repeatedly exhibited phenomena which fit that description.

In view of all the unexplained facts, the emission near 4680 Å constitutes a significant and interesting theoretical problem. Like many other outstanding puzzles involving η Car, it may relate to several branches of astrophysics and deserves careful attention.

7. Acknowledgments

We are grateful to M. Feast for re-inspecting Thackeray’s spectra of Eta Carinae for us. We thank O. Stahl, K. Weis, and the Eta Carinae UVES Team for their continued collaboration and sharing of data. We also thank K. Nielsen and G. Vieira-Kober for providing us with the reduced and extracted STIS/MAMA spectra. We acknowledge M. Corcoran for providing many constructive comments and discussion regarding an early draft. Additionally, we are grateful to T.R. Gull and Beth Perriello for preparing the HST observing plans. T.R. Gull prepared most of the detailed STIS observing plans and gave other valuable help in the Treasury Program. We also especially thank J.T. Olds, Matt Gray, and Michael Koppelman at the University of Minnesota for helping with non-routine steps in the data preparation and analysis.

The HST Treasury Project for Eta Carinae is supported by NASA funding from STScI (programs GO-9420 and GO-9973), and in this paper we have employed HST data from several earlier Guest Observer and Guaranteed Time Observer programs. Treasury Project co-investigators who opted not to participate in this particular paper are T. Gull, S. Johans-

¹²Strictly speaking, in their scenario the secondary star is eclipsed by the high density primary wind extended along the polar axis, not by the primary star itself; but this distinction is unimportant here.

son, N. Walborn, M. Bautista, F. Hamann, M. Corcoran, and H. Hartman.

This work also made use of the NIST Atomic Spectra Database¹³ and the Kentucky Atomic Line List v2.04¹⁴.

¹³http://physics.nist.gov/cgi-bin/AtData/main_asd

¹⁴<http://www.pa.uky.edu/~peter/atomic/index.html>

REFERENCES

Cardelli, J. A., Clayton, G. C., & Mathis, J. S. 1989, *ApJ*, 345, 245

Corcoran, M. F., et al. 2001, *ApJ*, 562, 1031

Corcoran, M. F., et al. 2004, *ApJ*, 613, 381

Corcoran, M. F. 2005, *AJ*, 129, 2018

de Vaucouleurs, G. & Eggen, O. J. 1952, *PASP*, 64, 185

Damineli, A. 1996, *ApJ*, 460, L49

Davidson, K., & Netzer, H. 1979, *Revs. Mod. Phys.* 51, 715

Davidson, K. & Humphreys, R. M. 1997, *ARA&A*, 35, 1

Davidson, K. 1999, *Astronomical Society of the Pacific Conference Series*, 179, 304

Davidson, K., Ishibashi, K., Gull, T. R., Humphreys, R. M., & Smith, N. 2000, *ApJ*, 530, L107

Davidson, K. 2002, *Astronomical Society of the Pacific Conference Series*, 262, 267

Davidson, K. 2004a, *STScI Newsletter*, Spring 2004, 1

Davidson, K. 2004b, “Our Adopted Scheme for Subpixel Modeling,” University of Minnesota Eta Carinae Treasury Project Team Technical Memo #1, <http://etacar.umn.edu/treasury/techmemos/pdf/tmemo001.pdf>

Davidson, K., Martin, J. C., Humphreys, R. M., Ishibashi, K., Gull, T. R., Stahl, O., Weis, K., Hiller, D. J., Damineli, A., Corcoran, M., & Hamann, F. 2005a, *AJ*, 129, 900

Davidson, K. 2005b, “The Meaning of ”ERR” HDU’s or Noise Files,” University of Minnesota Eta Carinae Treasury Project Team Technical Memo #7, <http://etacar.umn.edu/treasury/techmemos/pdf/tmemo007.pdf>

Davidson, K. 2005c, *Astronomical Society of the Pacific Conference Series*, 332, 103

Fitzpatrick, E. L. 1999, *PASP*, 111, 63

Feast, M., Whitelock, P., & Marang, F. 2001, *MNRAS*, 322, 741

Gaviola, E. 1953, *ApJ*, 118, 234

Gull, T. 2005, Astronomical Society of the Pacific Conference Series, 332, 281

Hamaguchi, K., Corcoran, M. F., Gull, T., White, N. E., Damineli, A., & Davidson, K. 2004, ArXiv Astrophysics e-prints, astro-ph/0411271, to appear in “Massive Stars in Interacting Binaries” held in Quebec Canada (16-20 Aug, 2004)

Hillier, D. J., Davidson, K., Ishibashi, K., & Gull, T. 2001, ApJ, 553, 837

Hillier, D. et al. 2005, in preparation

Humphreys, R. M., & Koppelman, M. 2005, Astronomical Society of the Pacific Conference Series, 332, 161

Ishibashi, K., Corcoran, M. F., Davidson, D., Swank, J. H., Peetre, R., Drake, S. A., Damineli, A., & White, S. 1999, ApJ, 525, 983

Johnson, H. M. 1968, in Stars and Stellar Systems, Chicago: University of Chicago Press, 1968, edited by Middlehurst, Barbara M.; Aller, Lawrence H., 65

Lamers, H. J. G. L. M., & Cassinelli, J. P. 1999, Introduction to Stellar Winds / Henny J.G.L.M. Lamers and Joseph P. Cassinelli. Cambridge ; New York : Cambridge University Press, 1999. ISBN 0521593980, p.211

McKenna, F. C., Keenan, F. P., Hambly, N. C., Allende Prieto, C., Rolleston, W. R. J., Aller, L. H., & Feibelman, W. A. 1997, ApJS, 109, 225

Martin, J.C. 2005, Astronomical Society of the Pacific Conference Series, 332, 114

Meaburn, J., Wolstencroft, R. D., & Walsh, J. R. 1987, A&A, 181, 333

O’Connell, D. J. K. 1956, Vistas in Astronomy, 2, 1165

Osterbrock, D. E. 1989, Astrophysics of Gaseous Nebulae and Active Galactic Nuclei, (Mill Valley, CA: University Science Books)

Pittard, J. M. & Corcoran, M. F. 2002, A&A, 383, 636

Smith, N., Davidson, K., Gull, T. R., Ishibashi, K., & Hillier, D. J. 2003, ApJ, 586, 432

Stahl, O., Weis, K., Bohmans, D. J., Davidson, K., Gull, T. R., & Humphreys, R. M. 2005, A&A, in press.

Steiner, J. E., & Damineli, A. 2004, ApJ, 612, L133

Thackeray, A. D. 1953, MNRAS, 113, 211

Viotti, R. F., et al. 2002, A&A, 385, 874

Whitelock, P. A., Feast, M. W., Koen, C., Roberts, G., & Carter, B. S. 1994, MNRAS, 270, 364

Whitelock, P. A., Feast, M. W., Marang, F., & Breedt, E. 2004, MNRAS, 352, 447

Zanella, R., Wolf, B., & Stahl, O. 1984, A&A, 137, 79

A. Line Identification of 4680Å

The likely identification of the 4680Å feature is He II λ 4687.0. If this is correct, then other He II recombination lines should also be present. A summary of the strongest expected He II transitions is given in Table 2. Other transitions exist in the infrared, but our data do not extend beyond 10128Å.

Unfortunately, several factors conspire to make the detection of these lines difficult. These obstacles include: extinction (mostly circumstellar), blends with other spectral features (esp. hydrogen Balmer lines), and relative weakness of most of the transitions. As an example, assuming a typical excitation process, He II λ 1640 should be more than eight times the strength of He II λ 4687. However, it is not detected in the MAMA/Echelle data (Gull 2005). This may be understandable since the spectrum at these wavelengths is complicated by several strong overlapping absorption complexes (Gull 2005; Hillier et al. 2005). If the UV absorption were so thick as to block He II λ 1640 completely, then one might naively expect no detectable flux from the star around 1640 Å. However, there is some flux (on the order of $2 - 6 \times 10^{-12}$ erg cm $^{-2}$ s $^{-1}$ Å $^{-1}$) which the MAMA detects around 1640Å unresolved from the central star. Hillier et al. (2005) explains this flux as UV continuum which is attenuated by a factor of at least one hundred and forms between 10 and 20 AU from the central star. Therefore, the absence of He II λ 1640 indicates that the origin of the He II emission is probably at a much deeper optical depth, much closer to the central star.

One should note that if the region of He II emission moves with the secondary star (Steiner & Damineli 2004), then as the secondary travels further from the primary on its highly elliptical orbit, it will pass into a region with smaller optical depth. If the He II emission occurs continuously throughout the cycle as claimed by Steiner & Damineli then we would have a much better chance of detecting He II 1640 Å when the secondary is furthest

from the primary, near apasteron. However, our only mid-spectroscopic cycle MAMA E140M observation (2000 March 23; MJD 51267.3) shows no more evidence of He II λ 1640 emission than the other spectra observed throughout the cycle.

Because of UV extinction and blending with Balmer lines, He II λ 5413 and He II λ 10126 are the two transitions which we have the best chance of detecting in the STIS spectra. Assuming that the feature at 4680Å is He II λ 4687, then those lines should have similar profiles. In Figure 7 we have plotted the differences between the observed flux profiles at the time of maximum strength of the 4680Å feature (MJD 52813.8) and the average flux profiles when the 4680Å feature is not present, for the He II λ 10126, and He II λ 5413 compared with the He II λ 4687 profile scaled for comparison.

The He II λ 10126 emission line should be at least one quarter the strength of He II λ 4687 and may appear stronger since it should typically be less affected by extinction. In the top panel of Figure 7, we scaled the He II λ 10126 flux profile by a factor of 0.60. This corresponds to an extinction at 10126Å of about one seventh the extinction at 4687Å which is consistent with the standard reddening curves of Fitzpatrick (1999) and Cardelli et al. (1989). The 10126Å data is also hampered by higher detector noise and higher uncertainty in the flux calibration because it falls near the physical edge of the CCD and the red limit of the STIS's spectral sensitivity. There is a significant increase in flux near He II λ 10126 on MJD 52813.8. However, the velocity profile is notably different from the 4680Å feature on that date (Figure 7).

He II λ 5413 is a weaker transition (0.08 the strength of He II λ 4687) with approximately the same extinction as He II λ 4687. In the bottom panel of Figure 7 the relative scale factor between the profiles is set to the relative strength of the transitions. The 5413Å flux profile is noisy but appears to have roughly the same velocity profile as 4687Å. However, the noise level in the 5413Å data negates the significance of any match with the expected profile.

Therefore, we conclude that we are unable to detect these or any additional He II lines in our data, but the limits do not exclude the λ 4687 identification. Given this fact, we can neither confirm or deny that the 4680Å feature is correctly identified as He II λ 4687. In such a situation it is prudent to examine the other options which are available.

A pair of N III lines near 4681Å might contribute to the feature. However, they are high excitation lines and our own inspection of the spectrum agrees with Thackeray (1953) that the species N III is “doubtfully present.” A cluster of Ne I lines from 4680Å to 4683Å might also be responsible for the observed emission, but almost no neutral Ne should be present in the stellar wind. There are also unidentified lines in the emission spectrum of the Orion Nebula at 4679.21Å (Johnson 1968) and in the spectrum of RR Tel at 4681.38Å (McKenna

et al. 1997) which may be related to our feature. However, it is difficult if not impossible to prove that this feature is positively related to another unidentified feature in another object that might not have the same physical conditions. Therefore, for the time being, we shall assume that the 4680Å emission feature in the spectrum of η Carinae is He II λ 4687 because from a theoretical point of view He II is “more natural” than the alternatives.

B. Calculation of Errors & Detection Limits at Times When the Feature was not Detected

The HST/STIS data show no obvious emission near 4687 Å during 1998-2002 and after 2003.5 (Figure 3). However, Steiner and Damineli asserted that such emission is *usually* present with an equivalent width between 50 and 200 mÅ (see their Figure 2). A detailed quantitative assessment is needed to resolve this conflict.

The flux and equivalent width errors presented in Tables 1 and 2 were calculated from the signal-to-noise (S/N) in the extracted spectra. Here S/N was calculated from the ratio of average flux per pixel and the standard deviation of the flux per pixel in the patch of continuum between 4742.5 Å and 4746.5 Å. Within that wavelength range the pixel width is 0.276Å. (We use a different approach in Table 3, see below.) The pixels in our data have been interpolated so the raw S/N values were corrected for this factor. The noise in a flux measurement is then calculated as the quotient of that flux and S/N:

$$\text{Noise} = \text{Flux}/(\text{S}/\text{N})$$

The line fluxes in Table 1 are the difference between the total flux measured between 4675 Å and 4694 Å and the estimated continuum contribution. It follows that error in the line flux is the sum in quadrature of the total flux noise and the estimated continuum noise.

Equivalent width errors depend on both the flux and the feature’s profile because a line must peak above the noise level in order to be detected. In this work we assume, for convenience, that the feature has a Gaussian shaped profile. However, results are not very sensitive to this assumption. The errors in the equivalent widths (Table 1) are calculated using the following formula:

$$\sigma_{EW} = [3\lambda_0/2(\text{S}/\text{N})] \times (v_w/c)$$

where λ_0 is the line center, v_w is the Doppler width of the feature (which was taken to be 600 km s⁻¹, see Figure 2), and c is the speed of light.

The same assumptions are used to calculate the detection limit in Table 2 (Φ_{min}) from

the noise in the data(N):

$$\Phi_{min} = N\lambda_0\sqrt{2\pi} \times (v_w/c)$$

The noise level (σ) is obviously essential for determining whether He II $\lambda 4687$ is present in emission outside the spectroscopic event. Regarding our extracted spectra, which are essentially sums of about 5 CCD rows, we define σ as the ratio (r.m.s. noise)/(continuum level) for a wavelength sample 0.276 Å wide, the STIS/CCD column width. Experience shows that it is not safe to rely on instrumental count-number statistics (e.g., in the standard FITS ERR arrays, see Davidson (2005b)) for estimating this quantity. Therefore we have used two methods to estimate σ from the fully processed spectral data in the wavelength range 4677–4693 Å: (1) The r.m.s. difference between independent wavelength samples in an extracted spectrum, $f(n+m) - f(n)$ where $m = 2, 3, 4$, and 5 CCD columns, is a measure of the noise. (2) We also used r.m.s. differences between the data and the least-squares fits described below. These two methods agreed with each other to better than 10% for every pertinent observation date (usually better than 6%), so we adopt their average as listed in Table 3. The relative σ in our data is typically close to 0.008 for a sample width of one STIS/CCD column; and of course the analysis described below uses many such columns.

The noise-estimation process includes subtle factors too lengthy to discuss here. For instance, in our measurements we used the standard Treasury Project data pixels, derived from the original CCD pixels by a special form of interpolation (Davidson 2004b). Because interpolation has been used, one must take into account the mathematical correlations between any pixels that are near each other. Moreover, inspection shows that an appreciable fraction of the estimated r.m.s. “noise” is not random but varies sinusoidally with a repetition period of typically 5 CCD columns. This “pattern noise” is different from the “scalloping” pattern which plagues very narrow STIS CCD one-dimensional spectral extractions from the STScI pipeline (Davidson 2004b). We included these and related effects in our calculations, and we used special random simulation programs to verify our mathematical assumptions.

A major obstacle to detecting weak He II $\lambda 4687$ emission is the limited width of the smooth continuum interval. Blueward of 4677.2 Å and redward of 4693.5 Å, unrelated emission features perturb the spectrum (Figure 1). Consequently the one-sigma uncertainty in E.W. for weak He II emission *in general*, with almost arbitrary profile, is about 100 or 150 mÅ as indicated in the last column of Table 3. However, if we test only for the type of emission profile reported by Steiner and Damineli – FWHM 500 to 600 km s⁻¹, central Doppler velocity between –250 and +150 km s⁻¹ – then the uncertainty becomes much smaller. We employed the following procedure:

- Include only data samples $f(\lambda_i)$ in the wavelength interval mentioned above.

- For each observation, suppose that each dataset can be represented by

$$f(\lambda) = A + B\lambda + C\phi(\lambda),$$

where $\phi(\lambda)$ is an assumed profile.

- In our main calculations we employed a Gaussian shape for $\phi(\lambda)$, with FWHM ≈ 550 km s $^{-1}$ and central velocity between -250 and $+150$ km s $^{-1}$. The outcome does not depend strongly on the precise shape and width of $\phi(\lambda)$.
- For each STIS observation we used a conventional least-squares technique to estimate A , B , and C . Coefficient C indicates the strength of the suspected emission feature.
- In one respect we deviated from proper statistical testing procedure. Instead of finding the central Doppler velocity that gave the best formal fit, we chose the largest value of C calculated for assumed velocities in the range -250 to $+150$ km s $^{-1}$. This obviously over-estimates the suspected emission, but for the present purpose (finding an upper limit) the effect is small.
- In order to assess the uncertainty in C , we performed many random numerical Monte Carlo simulations of the procedure. Under the conditions specified above, the r.m.s. uncertainty in the height of the putative emission feature turns out to be approximately half the r.m.s. noise value that applies to a 0.276 Å sample width (the CCD column width as noted earlier).

Results are listed in Table 3, mostly representing observation dates when the STIS data showed no obvious He II emission. The one exception, MJD 52683 early in 2003, is included merely to affirm that this method would indeed detect a weak emission feature. At first sight the equivalent width found for that date seems to conflict with the value listed in Table 1, 183 ± 45 mÅ vs. 330 ± 120 mÅ. In fact, however, there is no serious contradiction, since the emission observed at that time appears to have been broader than we assumed in Table 3 (i.e., it was broader than the “usual” feature described by Steiner and Damineli), while a relatively large uncertainty is stipulated in Table 1. We emphasize that the values listed in Tables 1 and 3 were obtained by two very different, largely independent methods; the former was fairly general, while the latter applies only to an emission feature with the characteristics that Steiner and Damineli reported for 1998–2002 and post-2003.50.

Aside from the 2003.12 observation, Table 3 shows no evidence for He II emission before 2003 and after 2003.50, over the rest of the spectroscopic cycle. A typical individual observation allows an equivalent width of roughly 40 mÅ at the one-sigma level and, of course, twice as large at the two-sigma level; but here we have eleven independent observations, not one. Their average E.W. is practically zero with a formal error of the order of ± 11 mÅ. (Incidentally, the r.m.s. dispersion of these eleven values is 38 mÅ, satisfactorily consistent with the uncertainties estimated from the individual data sets.) The last line in Table 3 shows the result of our procedure applied to the average of all eleven spectra (each normalized so

the average level is unity). This differs from the average of the individual calculated results, because they do not all refer to the same Doppler velocity for $\phi(\lambda)$.

In summary, the STIS data do not support the assertion by Steiner and Damineli that He II emission is usually present with an equivalent width in the range 50–200 mÅ. Unfortunately those authors did not show a tracing of the feature during the time intervals in question, nor did they clearly specify the noise level in their data. (Their quoted S/N ratio is not accompanied by a $\Delta\lambda$ that it refers to.) Our STIS data have the obvious advantage of good spatial resolution, which reduces contamination by bright ejecta near η Carinae. Steiner & Damineli's exact spatial resolution has not been specified, but we assume that it was most likely 2'', including both seeing and the spectrograph aperture size. Their data have better spectral resolution than STIS, but that has practically no effect in this case which involves only broad spectral features. Altogether, we conclude that during most of the 5.5-year spectroscopic cycle, He II emission from the star (or rather, from gas within 100 AU of it) is substantially fainter than the values they reported. If such emission arises at larger radii to explain the discrepancy, then presumably a separate emission process must be responsible. However, one should also note that the VLT/UVES spectra detected no extended emission along their slit outside the spectroscopic event (Stahl et al. 2005).

C. Mapping the Emission Region

We can take advantage of the superior spatial resolution offered by the Hubble Space Telescope to constrain and map the extent of the 4680 Å emission. The feature was present with sufficient strength to measure its cross-dispersion profile in four spectra between MJD 52764.3 and MJD 52813.6. Each of those spectra show that the 4680 Å emission is confined inside the same area as continuum emission around the central star with no detectable change in the size or shape of the emission region over time. The slit positions for these spectra are roughly aligned with the presumptive equatorial or “orbital plane” of Eta Carinae (slit orientations: 70°, 62°, 38°, and 27° measured from north through east).

While a single STIS spectrum measures the size and position of the 4680 Å emission region in only one-dimension, the source of the emission may be extended in the dispersion direction and we would be unable to tell from a single spectrum. However, multiple spectra gathered by slits with different positions and orientations can be combined to create a two-dimensional map of the emission region. During the period when 4680 Å emission was strong, there were three additional observations with the same wavelength coverage and similar slit orientations as the four spectra targeted on the central source. Those additional spectra are centered on Weigelt blob D and therefore provide additional spatial coverage to the

northwest of the central source. By combining these seven STIS observations, we are able to map out the region of 4860 Å emission more extensively than we could do with a spectrum from a single slit (Figure 8).

The image map generated by combining the slits is smeared diagonally from lower left to upper right because there is no spatial resolution for an individual spectrum in the dispersion direction. However, it is still obvious that the 4680 Å emission is tightly confined to the same region as the continuum, with no evidence of any extended emission along the equatorial axis or within 0.2" of the central star to the northwest. It is still possible that the 4680 Å emission is extended only in the southeast direction, but this configuration would be contrived.

If a significant source of extended emission is responsible for the differences between the spectra observed by the STIS and Steiner & Damineli (2004) then the source of this emission is probably at much larger radii on the polar axis. However, examination of spectra outside of the spectroscopic event (some of which have slit orientations aligned with the polar axis) also show no extended emission.

D. Intrinsic Luminosity of the Observed Emission Feature

Eta Car's large and uncertain circumstellar extinction makes it difficult to convert the observed He II λ 4687 flux directly to an intrinsic luminosity. Fortunately, however, the star's intrinsic brightness is known to a useful accuracy, independent of the circumstellar extinction. Therefore the best approach is to use the underlying stellar continuum as a calibration reference. Based on theoretical considerations as well as the spatial resolution of STIS, we assume that the λ 4687 emission originates in the dust-free region within about 150 AU of the star. Steiner & Damineli (2004) estimated the continuum brightness from a theoretical model of η Car's wind, but that approach seems unsafe to us because it requires a number of implicit, mostly unexpressed assumptions. We prefer to use η Car's brightness observed 200 to 400 years ago, before the Great Eruption produced the circumstellar extinction. This approach requires two critical assumptions: that the star's luminosity has not changed much, and that circumstellar extinction was small before 1800. Both seem consistent with all available theoretical and observational data.

Before 1800 the star varied between fourth and second magnitude at visual wavelengths, with (probably) little change in total luminosity. In the fainter state, the continuum resembled a hot star with a relatively transparent wind; and the second-magnitude state occurred whenever the wind became dense enough to form a photosphere cooler than 9000 K (Davidson & Humphreys 1997). The present-day state of the wind is closer to the hotter case, but,

most likely, with a somewhat increased mass-loss rate; therefore the brightness would now be third or fourth magnitude if the circumstellar extinction were not present. We adopt $V \approx 3.5$, which implies $V_0 \approx 2.0$ when corrected for interstellar extinction. The r.m.s. uncertainty is perhaps 0.5 magnitude, but this is non-Gaussian in the sense that an error worse than about 0.8 magnitude seems very unlikely. If the intrinsic color is $(B - V)_0 \approx -0.1$ based on the wind's spectroscopic character (this detail does not strongly affect our result), and if $D \approx 2.3$ kpc, then η Car's intrinsic luminosity per unit wavelength near 4687Å is about 6×10^{35} erg s⁻¹ Å⁻¹. This is about 40% larger than Steiner and Damineli's calibration, a reasonable agreement in view of the uncertainties.

Therefore an emission equivalent width of 1 Å corresponds to intrinsic luminosity $L(\lambda 4687) \approx 6 \times 10^{35}$ erg s⁻¹ or 1.4×10^{47} photons per second. If this is an *over*-estimate worse than a factor of about two, then some underlying assumption that we share with Steiner & Damineli (2004) must be fundamentally incorrect – which would be interesting in itself.

As discussed in Section 3, the STIS data indicate that the He II $\lambda 4687$ equivalent width briefly exceeded 2 Å around MJD 52813.8 (Table 1, Fig.2), with a very broad velocity dispersion. This value corresponds to $L(\lambda 4687) > 10^{36}$ erg s⁻¹, an impressive amount even if we were to reduce it by a factor of two or three merely for the sake of moderation.

E. Indirect Amplification by He II $\lambda 304$

In a He⁺⁺ region, trapped $\lambda 304$ resonance photons (He⁺ 1s–2p) greatly increase the population of the He⁺ $n = 2$ level. This fact can enhance the $\lambda 4687$ (3–4) emission in several ways:

1. Since the ionization potential from level 2 is only 13.6 eV, ordinary stellar UV radiation may contribute to the ionization, increasing the extent of the He⁺⁺.
2. If the optical depth for the 2–4 transition is appreciably larger than unity, then direct decay from level 4 to level 2 becomes ineffective because the resulting 1215.2 Å photons cannot easily escape. In that case, unlike a low-density nebula, almost every “successful” decay from level 4 goes through level 3, producing a $\lambda 4687$ photon. This is “nebular case C” in the same sense as the more familiar “case B.”
3. Trapped hydrogen L α photons may excite He⁺ ions from level 2 to level 4. (Stellar continuum photons may also cause 2–4 excitations, but they must be estimated in a different way so we discuss them separately in Appendix G.)

Let us suppose that the region of interest, within a stellar wind, is expanding with local velocity gradient $dv/dx = \eta$ averaged over directions. Then, *à la* Sobolev, the optical thickness in the $\lambda 304$ feature along a straight path through the region is

$$\tau_{\lambda 304} \approx \frac{(3.4 \times 10^{-8} \text{ cm}^3 \text{ s}^{-1}) n_1}{\eta}, \quad (\text{E1})$$

where n_1 is the density of He^+ ions in the 1s level at the location that contributes most strongly to the path integral; this is fairly well defined if the local turbulent and thermal velocity dispersion is not too large. The constant factor in eqn. E1 involves the oscillator strength. In normal circumstances $\tau_{\lambda 304} \gg 1$, and the average escape probability for a $\lambda 304$ photon is $\Pi \approx 1/\tau_{\lambda 304}$ per scattering event (see Section 8.5 in Lamers & Cassinelli (1999)). *Caveat:* By assuming simple homogeneous expansion, we are consciously optimizing the entrapment of resonance photons. Local instabilities and small-scale velocity gradients may decrease the effects discussed below, possibly by large factors.

Consider the equilibrium densities of the $n = 1$ and $n = 2$ levels of He^{++} in the He^{++} region. Critical parameters are:

- $R_{c2} \approx \alpha_B n_e n(\text{He}^{++})$, the effective recombination rate per unit volume. Here we use α_B , the standard recombination rate passing through level 2. Although we do not discuss this detail here, α_B is a good approximation in the parameter range of interest.
- A_{1c} , the X-ray photoionization rate per ion from level 1 ($\epsilon > 54.4$ eV). Note that the photoionization cross-section decreases rapidly with photon energy, roughly $\sigma(\epsilon) \propto \epsilon^{-3}$.
- A_{2c} , the UV photoionization rate from level 2 ($\epsilon > 13.6$ eV); this depends on the Lyman continuum of the primary star, the secondary star, or both.
- $A_{21} \approx 7.5 \times 10^9 \text{ s}^{-1}$, the $\lambda 304$ decay rate. Here “level 2” includes both 2s and 2p, since collisional transitions strongly mix them at relevant densities.

Other effects, e.g., collisional de-excitation from level 2 to level 1, are negligible for our purposes. The equilibrium equations then lead to the following densities:

$$n_1 \approx \left(\frac{\Pi A_{21}}{\Pi A_{21} + A_{2c}} \right) \frac{R_{c2}}{A_{1c}} \approx \left(\frac{A_{21}}{A_{21} + A_{2c} \tau_{\lambda 304}} \right) \frac{R_{c2}}{A_{1c}} \quad (\text{E2})$$

and

$$n_2 \approx \frac{A_{1c}}{\Pi A_{21}} n_1 \approx \frac{A_{1c} \tau_{\lambda 304}}{A_{21}} n_1. \quad (\text{E3})$$

If we define a dimensionless quantity

$$\xi = \frac{(3.4 \times 10^{-8} \text{ cm}^3 \text{ s}^{-1}) R_{c2} A_{2c}}{\eta A_{21} A_{1c}}, \quad (\text{E4})$$

then eqns. E1, E2, and E3 together imply

$$n_1 \approx \frac{2}{(1 + \sqrt{1 + 4\xi})} \frac{R_{c2}}{A_{1c}}, \quad (\text{E5})$$

$$n_2 \approx \frac{4\xi}{(1 + \sqrt{1 + 4\xi})^2} \frac{R_{c2}}{A_{2c}}. \quad (\text{E6})$$

With these densities, the optical depths in the 1–2 and 2–4 transitions turn out to be

$$\tau_{\lambda 304} \approx \left(\frac{2\xi}{1 + \sqrt{1 + 4\xi}} \right) \frac{A_{21}}{A_{2c}}, \quad (\text{E7})$$

$$\tau_{\lambda 1215} \approx \frac{1.13 A_{1c}}{A_{21}} \tau_{\lambda 304}^2. \quad (\text{E8})$$

We shall find that $\xi \gtrsim 1$ is required for strong enhancement of $\lambda 4687$ emission. This parameter depends on location within the He^{++} region; $\tau_{\lambda 304}$ and $\tau_{\lambda 1215}$ are “local” quantities because they refer to the local Doppler velocity in the expanding medium, in the standard Sobolev manner.

Now let us review the enhancement effects. If $\xi > 2$, then $A_{2c} > \Pi A_{21}$ in eqn. E2, and most of the photoionization is caused by UV acting on level 2. In effect the $\lambda 304$ photons amplify the spatial extent of the X-ray ionization, by tapping the stellar UV radiation field. The local amplification factor is

$$q_1 = \frac{A_{1c} n_1 + A_{2c} n_2}{A_{1c} n_1} \approx \frac{1 + \sqrt{1 + 4\xi}}{2}. \quad (\text{E9})$$

Next, one finds that $\tau_{\lambda 1215}$, the optical depth for He^+ 2–4 transitions, can be substantial. Then “case C” rather than “case B” describes the He^+ recombination cascade as mentioned earlier; so we have a second enhancement factor for the He II $\lambda 4687$ production efficiency compared to standard low-density nebular formulae. An adequate approximation is

$$q_2 \approx \frac{1 + 0.44 \tau_{\lambda 1215}}{1 + 0.26 \tau_{\lambda 1215}}. \quad (\text{E10})$$

Meanwhile, trapped hydrogen $\text{L}\alpha$ photons with suitable Doppler shifts can excite He^+ from level 2 to level 4, with rate A_{24} . Since $\tau_{\lambda 1215}$ is large wherever this effect is significant, we

can assume that a $\lambda 4687$ photon results from every such event. The production rate per unit volume is therefore $n_2 A_{24}$. A useful way to write this, using eqn. E6 for n_2 , is

$$n_2 A_{24} = q_3 R_{c2}, \quad (\text{E11})$$

where

$$q_3 \approx \frac{4 \xi}{(1 + \sqrt{1 + 4\xi})^2} \frac{A_{24}}{A_{2c}}. \quad (\text{E12})$$

We estimate A_{24} in Appendix F.

Taking these effects into account, the ratio of He II $\lambda 4687$ photons to X-ray photoionization events is approximately

$$Q_{\text{eff}} \approx (0.2 q_2 + q_3) q_1, \quad (\text{E13})$$

where the factor 0.2 is the corresponding production efficiency in the standard low-density case where $\xi \ll 1$. At a given location in the He⁺⁺ region, Q_{eff} can be estimated from eqns. E9, E10, and E12.

Since Q_{eff} is a local quantity, in order to take a valid average we must explore models of the He⁺⁺ region. Fortunately a simplified geometrical structure is adequate for plausibility assessments. Imagine, for example, a configuration illuminated from one side by soft X-rays – crudely representing “zone 4” in Fig. 6. Because the lowest-energy photons tend to be absorbed first, the ionization rate A_{1c} decreases with increasing depth into the region. With any reasonable ionizing spectrum, A_{1c} has a stronger gradient than the other quantities in eqn. E4; therefore ξ increases with depth. Thus the $\lambda 4687$ enhancement factors tend to be largest in regions where only the higher-energy photons penetrate, typically $\epsilon \gtrsim 250$ eV. Provided that the gas density is not too strongly correlated with depth in the region, local values of ξ and Q_{eff} are essentially determined by the average energy ϵ of photons being absorbed there; consequently, the large-scale shape of the He⁺⁺ region – plane-parallel, convex, concave, etc. – does not strongly affect the main results. Therefore, idealized plane-parallel models appear adequate to estimate Q_{eff} within a factor of two or most likely better. We calculated such models with the following assumptions:

- The region of interest is located near $r \sim 2.5$ AU relative to the primary star. This does not appear explicitly in the formulae, but it influences our choices of the other parameters. In a binary model, $r \sim 2.5$ AU is nearly optimum for the enhancement effects; smaller values of r would require extreme orbital eccentricities and very rapid periastron passage, while larger r implies smaller densities (see below).
- The expansion parameter is $\eta \approx 0.8 V_{\text{wind}}/r \approx 10^{-6} \text{ s}^{-1}$. The true value cannot be appreciably smaller than this near $r \sim 2.5$ AU in the expanding wind, while larger

values inhibit the $\lambda 304$ entrapment by decreasing the ξ -values.¹⁵ We shall say more about parameter dependences later below.

- The electron density is $n_e = (10^{10.5} \text{ cm}^{-3}) \mu$, where μ is an adjustable parameter. Note that μ is of the order of unity in a wind-disturbance model but $\mu \sim 0.1$ in the Pittard & Corcoran (2002) colliding-wind X-ray model. We also assume that the helium density is $0.15 n_e$, appropriate for η Car.
- Consistent with the adopted densities, the local He^{++} recombination rate per unit volume is $R_{c2} = (10^8 \text{ cm}^{-3}) \mu^2$. This is appropriate for a gas temperature around 30000 K; and different temperatures can be represented by small adjustments to μ . Inhomogeneities in the wind tend to increase the volume-averaged value of μ^2 but they also increase local values of η ; here we ignore this detail because other uncertainties are worse.
- The incident energy flux of photons between 54 eV and 550 eV is $\int F_\epsilon d\epsilon = (5 \times 10^{21} \text{ eV cm}^{-2} \text{ s}^{-1}) \chi$, where χ is another adjustable parameter which we take to be unity in most of our calculations. If $\chi = 1$, the total flux between 54 eV and 550 eV is $10^{37} \text{ ergs s}^{-1}$ in an area of 5.6 AU^2 .
- The spectrum between 54 and 550 eV has shape $F_\epsilon = \text{constant}$, while photons above 550 eV are absorbed by nitrogen instead of helium (and, therefore, may be converted to lower-energy photons which are included in our χ parameter). A more realistic spectrum shape would emphasize lower photon energies, thus decreasing the $\lambda 4687$ enhancement effects.
- We assume that the rate for ionization from $n = 2$ by stellar UV photons is $A_{2c} \approx 10^{4.1} \text{ s}^{-1}$, which seems realistic for either a binary or a single-star model.
- $A_{21} = 7.5 \times 10^9 \text{ s}^{-1}$ for He^+ , a standard atomic parameter.
- A_{24} , representing excitation by trapped hydrogen $\text{Ly}\alpha$ photons, is given by formula F4 in Appendix F. We also calculated models with $A_{24} = 0$.

¹⁵Incidentally, if the spatial thickness of the He^{++} region is less than about $(5 \text{ km s}^{-1})/\eta \sim 0.03 \text{ AU}$, then the resonance photon escape probability Π depends on the turbulent and thermal velocity dispersion, not on the expansion rate η . In that case one must use formulae in Section IV of Davidson & Netzer (1979) rather than $\Pi \approx 1/\tau$. This is another reason why the calculations used here tend to overestimate the enhancement effects. However, most of the $\lambda 4687$ enhancement occurs in “deep” zones of the He^{++} region, whose characteristic sizes are sufficiently large.

Figure 9 shows the resulting ratio of He II $\lambda 4687$ luminosity to the input soft X-ray luminosity, as a function of μ . This is a ratio of energy fluxes, not photon numbers. The upper curve includes excitation by $\text{L}\alpha$ as estimated in Appendix F; the lower curve omits that process. At least in principle, this figure suggests that $\lambda 304$ entrapment can induce an impressive amount of $\lambda 4687$ emission, possibly more than 10% of the soft X-ray luminosity if $\mu \gtrsim 1$. (In that case, of course, most of the energy supply comes from $\text{L}\alpha$ and the stellar UV radiation field, not from the X-rays. The latter are necessary to initiate the process, but then the effects discussed above amplify the results by large factors.) Equally important, *these processes are not strong enough to explain the observed $\lambda 4687$ emission if the relevant density is low*, $\mu \lesssim 0.25$. At moderately low densities the emission efficiency $F(\lambda 4687)/F(\text{soft Xrays})$ can be of the order of 0.01, which, though much higher than one would get without the enhancement effects, is not adequate to explain the observations – see Section 5. Apparently the effects discussed above can play a major role in a dense wind-disturbance or mass-ejection scenario as discussed in Section 5, but they are of little help in the lower-density colliding-wind model proposed by Pittard & Corcoran (2002) and advocated by Steiner & Damineli (2004).

Can the other variable parameters η , χ , and A_{2c} alter this assertion? Within the plausible ranges, we find that $F(\lambda 4687)/F(54 \text{ to } 550 \text{ eV})$ is approximately proportional to $\eta^{-0.5} \chi^{-0.45}$. The effect of the UV photoionization rate A_{2c} is more complex: For $\mu \approx 1$ the $\lambda 4687$ production rate is roughly proportional to $A_{2c}^{-0.7}$, for $\mu \approx 0.5$ the precise value of A_{2c} scarcely affects the results, and for $\mu \lesssim 0.25$ the enhancement factors increase with A_{2c} ; but the enhancement is insufficient in that case anyway. We also calculated some models with a pseudo-thermal factor $\exp(-\epsilon/500 \text{ eV})$ in the input spectrum, and found $\lambda 4687$ efficiencies about 20% less than in the models outlined above. In summary, μ is the dominant parameter.

Finally, we caution that realistic $\lambda 4687$ enhancement factors may be far less than we estimated above. Instabilities in the wind can produce local velocity gradients that help resonance photons escape. Moreover, any unrecognized process that destroys $\lambda 304$ or $\text{L}\alpha$ photons would also reduce the effects discussed here. Thus, in a sense we have derived *upper limits*.

F. $\text{L}\alpha$ and the A_{24} Rate

Hydrogen $\text{L}\alpha$ $\lambda 1215.7$ with a suitable wavelength shift can excite He^+ from its $n = 2$ level to $n = 4$ (1215.2 Å), and subsequent decay to $n = 3$ produces a $\lambda 4687$ photon. If we measure wavelength or frequency in terms of the Doppler parameter $v = (\lambda - \lambda_{\text{L}\alpha})/\lambda_{\text{L}\alpha}$, the He^+ 2–4 transition occurs at $v_{\text{HeII}} \approx -120$ km s $^{-1}$. Let us represent the $\text{L}\alpha$ radiation field by an equivalent temperature $T_{\text{rad}}(v)$, such that the photon energy density or average specific intensity at v is given by the Planck formula at that temperature. This equivalent temperature is determined by the hydrogen population ratio n_2/n_1 and by the optical depth at v . The resulting excitation rate for a He^+ ion in its $n = 2$ level is

$$A_{24}(\text{He}^+) \approx (5 \times 10^8 \text{ s}^{-1}) \exp\left(-\frac{118400 \text{ K}}{T_{\text{rad}}(v_{\text{HeII}})}\right), \quad (\text{F1})$$

based on the transition probability A_{42} for He^+ , statistical weights, and transition energy. Here we estimate $T_{\text{rad}}(v_{\text{HeII}})$ in the inner wind of η Car.

Again considering a region near $r \sim 2.5$ AU, we use the same expansion rate η and gas density parameter μ as in Appendix E, and the following rates for hydrogen:

- $R_{\text{H},c2} \approx \alpha_B n_e n(\text{H}^+) \approx 10^8 \mu^2 \text{ cm}^{-3} \text{ s}^{-1}$, the recombination rate through level 2. This is accidentally equal to the value that we used for helium in Appendix E, but the details differ. The temperature dependence is modest compared to other uncertainties, and can be incorporated in the density parameter μ .
- $A_{\text{H},1c} \sim 10^{4.4} \text{ s}^{-1}$, the photoionization rate from level 1. This is approximately equal to $1.8 A_{2c}(\text{He}^+)$ (Appendix E) because it involves the same UV flux between 13.6 and 24 eV.
- $A_{\text{H},2c} \approx 10^{5.8} \text{ s}^{-1}$, the photoionization rate from level 2. Since this involves mainly the primary star's flux in the Balmer continuum, it is less uncertain than $R_{\text{H},c2}$ and $A_{\text{H},1c}$.
- $A_{\text{H},21} \approx 4.7 \times 10^8 \text{ s}^{-1}$, the decay rate that produces $\text{L}\alpha$.

Collisional transitions mix levels 2s and 2p, other collisional transitions are negligible, etc. Most of the formulae in Appendix E apply to the trapped $\text{L}\alpha$ photons, except that for hydrogen we must replace eqn. E1 with

$$\tau_{\text{L}\alpha} \approx \frac{(1.34 \times 10^{-7} \text{ cm}^3 \text{ s}^{-1}) n_{\text{H},1}}{\eta}, \quad (\text{F2})$$

and $1.34 \times 10^{-7} \text{ cm}^3 \text{ s}^{-1}$ must be substituted for $3.4 \times 10^{-8} \text{ cm}^3 \text{ s}^{-1}$ in the formula analogous to eqn. E4. The latter then indicates that $\xi_{\text{H}} \approx 0.7 \mu^2$. For example, in a dense model

with $\mu \approx 1$ we find $\tau_{\text{L}\alpha} \approx 360$ and $n_{\text{H},2}/n_{\text{H},1} \approx 0.02$ which corresponds to an excitation temperature slightly above 22000 K. This means that T_{rad} is about 22000 K at any wavelength where $\text{L}\alpha$ is optically thick.

However, at $v_{\text{HeII}} \approx -120 \text{ km s}^{-1}$ the gas is probably *not* optically thick, since nearly all surrounding material has positive v relative to the location of interest. The wavelength difference is so large that the natural line wing dominates. Using the appropriate Lorentzian profile in the path integral that led to eqn. F2 for the line center, one finds an optical depth

$$\tau(v_{\text{HeII}}) \approx -\left(\frac{\lambda_{\text{L}\alpha} A_{\text{H},21}}{4\pi^2 v_{\text{HeII}}}\right) \tau_{\text{L}\alpha} \approx 10^{-4.8} \tau_{\text{L}\alpha} \approx 0.006. \quad (\text{F3})$$

Including this factor, $T_{\text{rad}}(v_{\text{HeII}})$ is reduced to only about 11400 K. A practical approximation for the resulting He^+ excitation rate is

$$A_{24}(\text{He}^+, \text{L}\alpha) \approx (23000 \text{ s}^{-1}) \left(\frac{A_{\text{H},1c}}{10^4 \text{ s}^{-1}}\right)^{-0.75} \mu^3 \approx (15000 \text{ s}^{-1}) \left(\frac{A_{2c}(\text{He}^+)}{10^4 \text{ s}^{-1}}\right)^{-0.75} \mu^3, \quad (\text{F4})$$

which agrees with our formulae to an accuracy better than 15% in the range $0.4 < \mu < 3$, $10^{3.9} \text{ s}^{-1} < A_{\text{H},1c} < 10^{4.9} \text{ s}^{-1}$. Larger values of μ are unlikely in this context, and for smaller values the excitation process is relatively weak.

G. Excitation by Stellar Radiation near 1215 Å

Stellar radiation near 1215.2 Å can excite He^+ from level 2 to level 4. The details are very different from excitation by trapped $\text{L}\alpha$ photons, because stellar radiation arrives from outside the He^{++} region. As a simple example, imagine a small sub-region with volume ΔV , illuminated by a beam of continuum radiation with flux F_λ . The gas in ΔV is expanding with rate η defined in Appendix E. If the Sobolev-style local optical depth $\tau_{\lambda 1215}$ is fairly large, one can show that the total amount of radiation scattered by He^+ in volume ΔV is approximately $(\lambda F_\lambda)(\eta \Delta V/c)$. This is extracted from a wavelength interval $\Delta\lambda$ that depends on the velocity dispersion within ΔV . Therefore, if $\tau_{\lambda 1215} \gtrsim 1$ in our η Car problem, then *the total rate of scattered photons is proportional to the volume of the He^{++} region*. In contrast to the effects described in Appendix E, this favors low-density cases. (If the density becomes too low, however, then $\tau_{\lambda 1215}$ becomes small.)

Consider incident radiation from the primary star, or rather from the opaque inner wind. Initially let us pretend that its luminosity spectrum is a smooth continuum L_λ . Suppose that every photon within Doppler interval $\Delta\lambda = \lambda \Delta v/c$ centered near 1215 Å, and within solid angle Ω , is intercepted by a He^+ ion in its $n = 2$ level and thereby converted to a photon

pair at 4687 and 1640 Å (the 4–3 and 3–2 decays). Then, relative to the star’s continuum, one can show that the equivalent width of the resulting pseudo-emission line at $\lambda 4687$ is

$$\text{EW}_\lambda(\lambda 4687) \approx (1215 \text{ Å}) \left(\frac{\Delta v}{c} \right) \left(\frac{\Omega}{4\pi} \right) S \approx (0.4 \text{ Å}) \left(\frac{\Delta v}{100 \text{ km/s}} \right) \left(\frac{\Omega}{4\pi} \right) S, \quad (\text{G1})$$

where

$$S = \frac{(\lambda L_\lambda)_{\lambda 1215}}{(\lambda L_\lambda)_{\lambda 4687}}. \quad (\text{G2})$$

For instance, the Planck formula would give $S = 0.56$ and 2.2 for $T = 15000$ K and 20000 K respectively. Considering that a $\text{L}\alpha$ absorption line is formed in innermost layers of the wind, it would be difficult for S to appreciably exceed 1 in the case of η Car. In a colliding-wind binary model, the spherical coverage factor $\Omega/4\pi$ is less than 0.1 and the applicable Δv is not likely to exceed 200 km s^{-1} even in a low-density model. Therefore the He II $\lambda 4687$ “emission” due to this process may have an equivalent width of the order of 0.1 Å near periastron, but not appreciably more.

The hypothetical companion star must be quite hot as discussed elsewhere; and, based on the lack of an impressive photoionized H II region in the inner Homunculus, its luminosity cannot be much more than 10% that of the primary. Combining these factors, its value of $L_\lambda(\lambda 1215)$ is less than 10% of the value for the continuum of the primary (or rather the primary’s inner wind), and most likely less than 5% . Therefore, even though its $\text{L}\alpha$ absorptions line is presumably weaker and its applicable covering factor $\Omega/4\pi$ might be as large as 0.5 rather than less than 0.1 , the secondary star cannot substantially increase the above estimate.

$\text{L}\alpha$ photons from the secondary wind are less important in this connection than the stellar radiation, because the hypothetical secondary wind is not particularly dense.

Since we have employed several uncertain parameters here, a model with different results seems possible though unlikely. More detailed calculations are obviously needed.

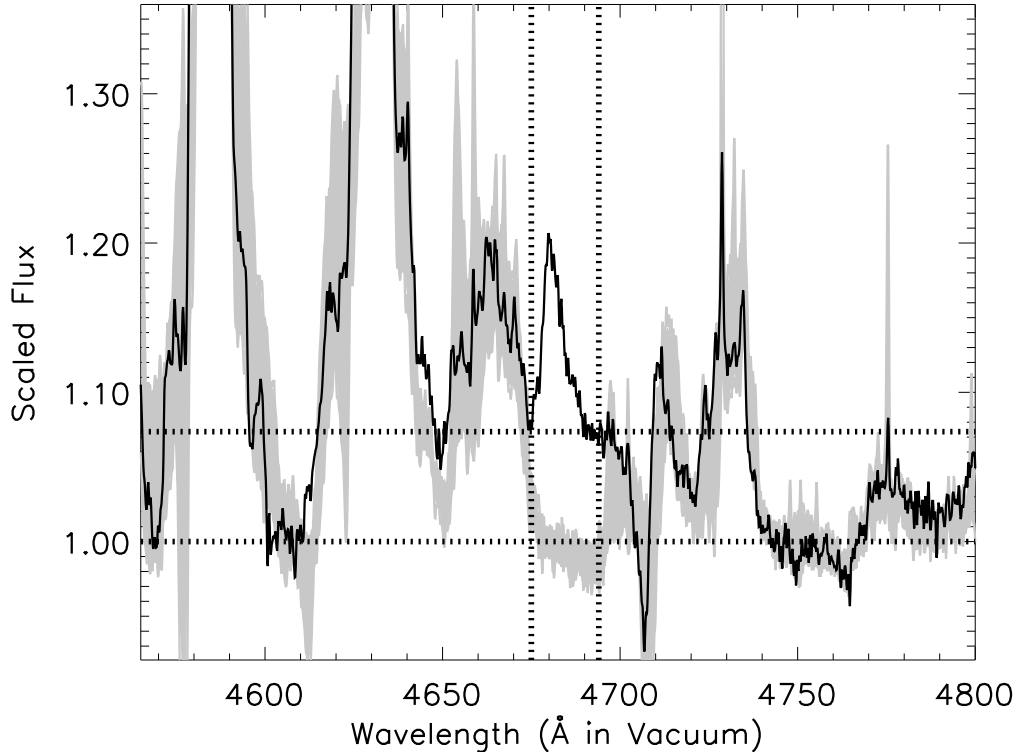


Fig. 1.— A demonstration of the effects which different adopted continuum levels have on the measured 4680 Å flux. The solid line is the spectral flux recorded on MJD 52813.8. The gray area is the range of *scaled* spectral fluxes when the 4680Å feature is not present. The vertical dotted lines are the flux integration limits for the 4680Å feature. The horizontal dotted lines are the continuum level estimated at 4744Å (lower line; scaled flux = 1.00) and the continuum level that one might assign if only data nearest to the feature is considered (upper line; scaled flux = 1.07). See also Figure 2.

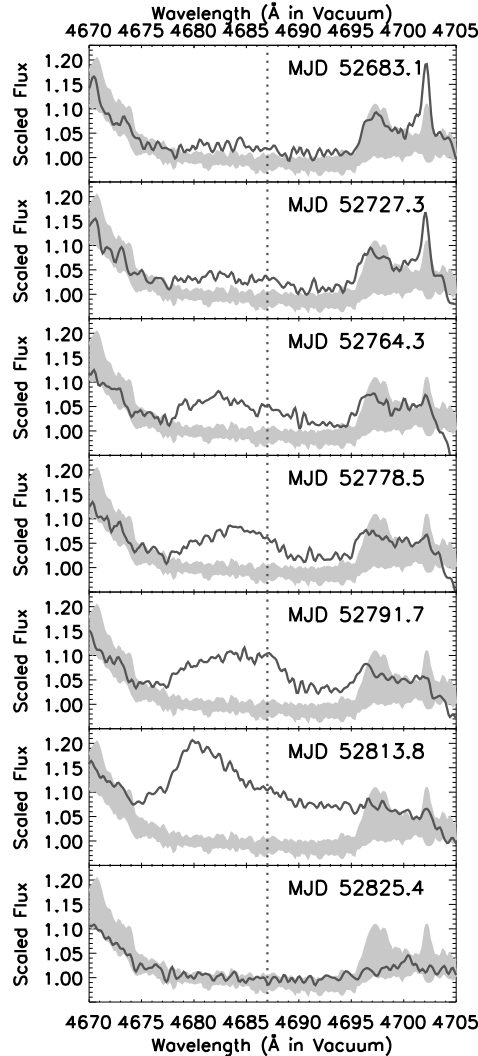


Fig. 2.— A time sequence showing the change in the 4680Å emission feature. The solid line is the scaled flux on that MJD (continuum flux = 1). For comparison, the gray envelope is the range of scaled fluxes observed when the 4680Å feature was not present. These tracings have not been smoothed.

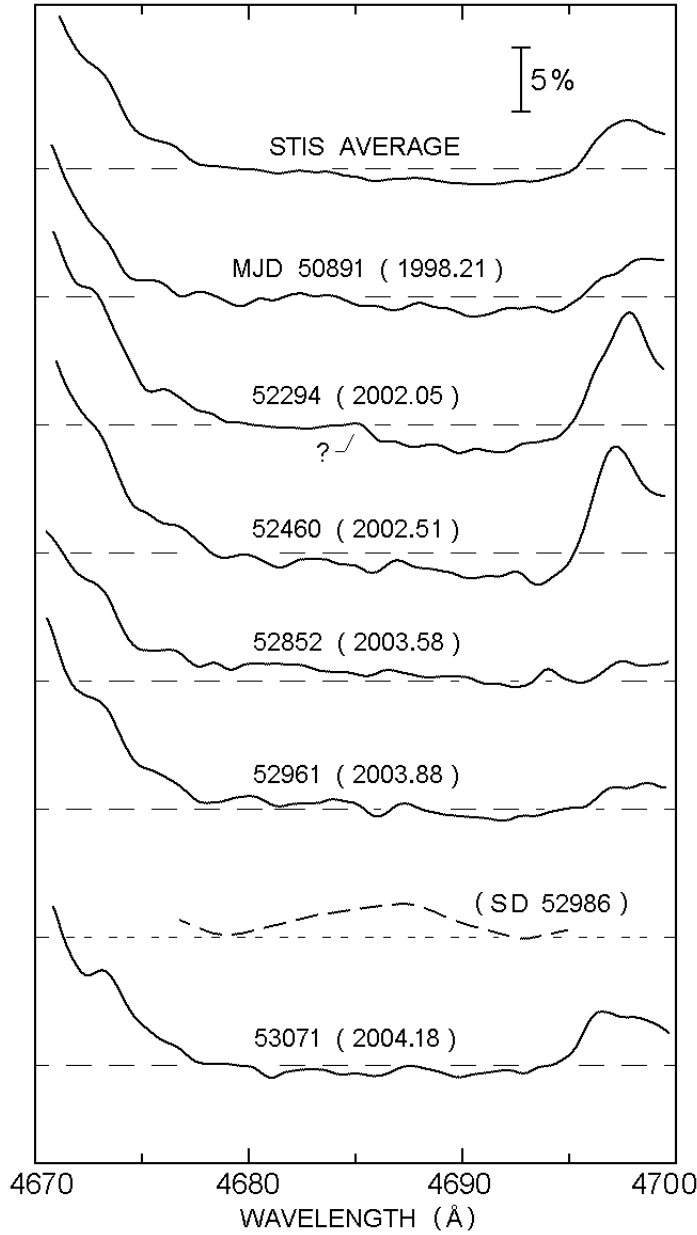


Fig. 3.— A sampling of STIS/CCD spectra from times when 4680 \AA was not present. These were smoothed with $\Delta\lambda \approx 0.5 \text{ \AA}$. At the top is the average scaled flux of these data. Second from the bottom is the spectrum reported by Steiner & Damineli (2004) on MJD 52986 when we detect no trace of the feature. The dashed horizontal lines denote the continuum as determined by the average flux between 4742.5 \AA and 4746.5 \AA . For a quantitative analysis see Appendix B.

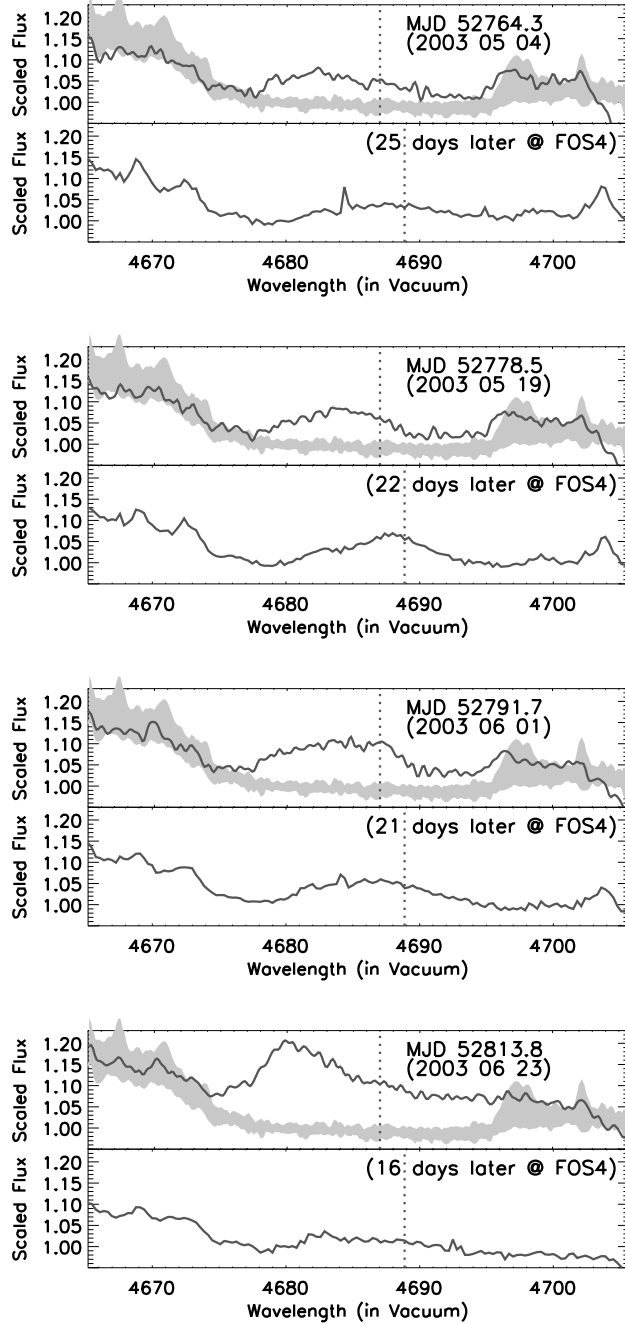


Fig. 4.— A comparison of the STIS spectrum (top panel of each set) of the central star with a corresponding VLT/UVES spectrum at a location in the Homunculus labeled FOS 4 (bottom panel of each set), with the delay noted (picked to be comparable to the estimated 20 day difference introduced by light travel time). Adjacent pixels in the VLT/UVES data have been combined so that data is plotted with the same spectral resolution as the STIS data ($\Delta\lambda \approx 0.3 \text{ \AA}$). The gray envelope plotted with the STIS data is the same as in Figure 2. The vertical dotted line marks the rest wavelength of He II $\lambda 4687$ in the STIS data and is shifted in the VLT/UVES spectrum to the velocity of the reflecting ejecta.

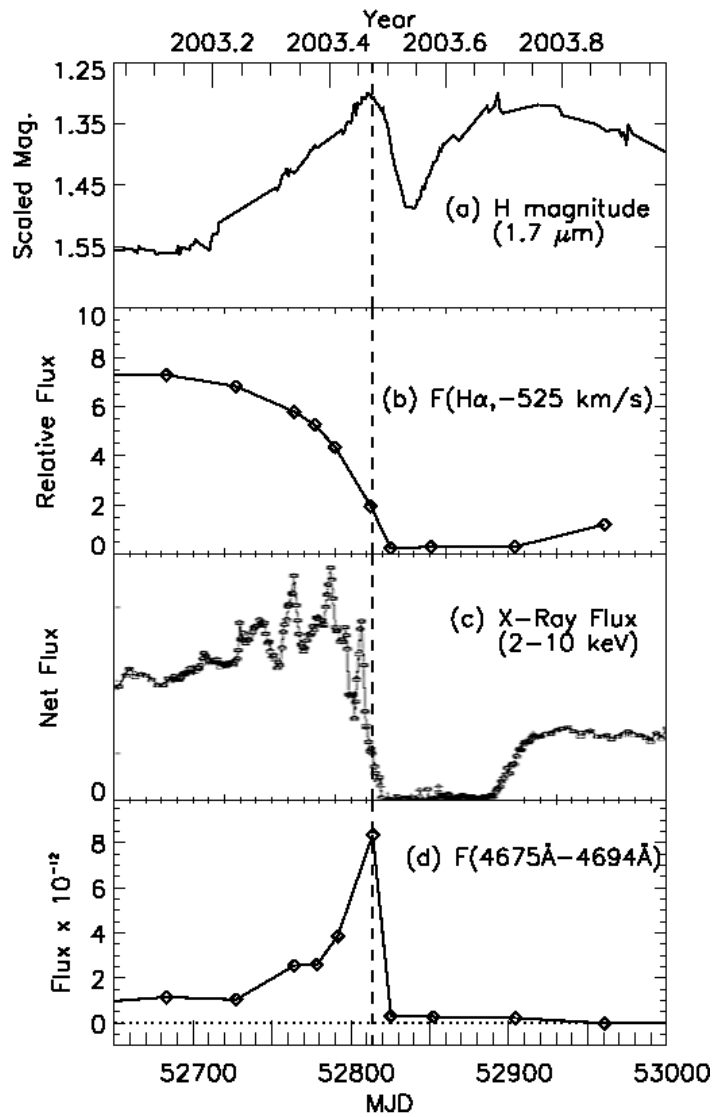


Fig. 5.— A comparison of the temporal evolution of the 4680 \AA emission feature strength (d) relative to: the near infrared H magnitude brightness (Whitelock et al. 2004) (a), the strength of the H α P-Cygni absorption (Davidson et al. 2005a) (b), and the 2–10 keV X-ray flux (Corcoran 2005) (c).

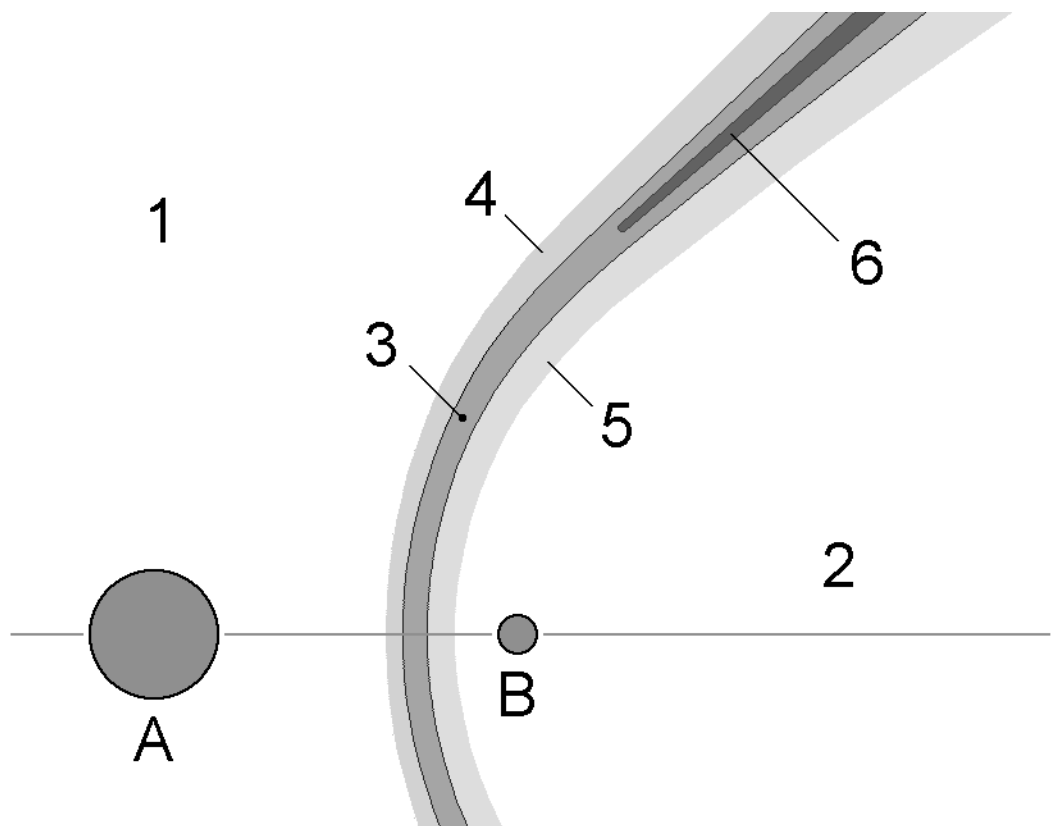


Fig. 6.— Schematic classification of ionization zones that may exist in the wind-wind interface between the primary (A) and hypothetical secondary (B) stars. See text for a full explanation. In reality the shock fronts and regions probably do not have simple geometries and they certainly vary with time.

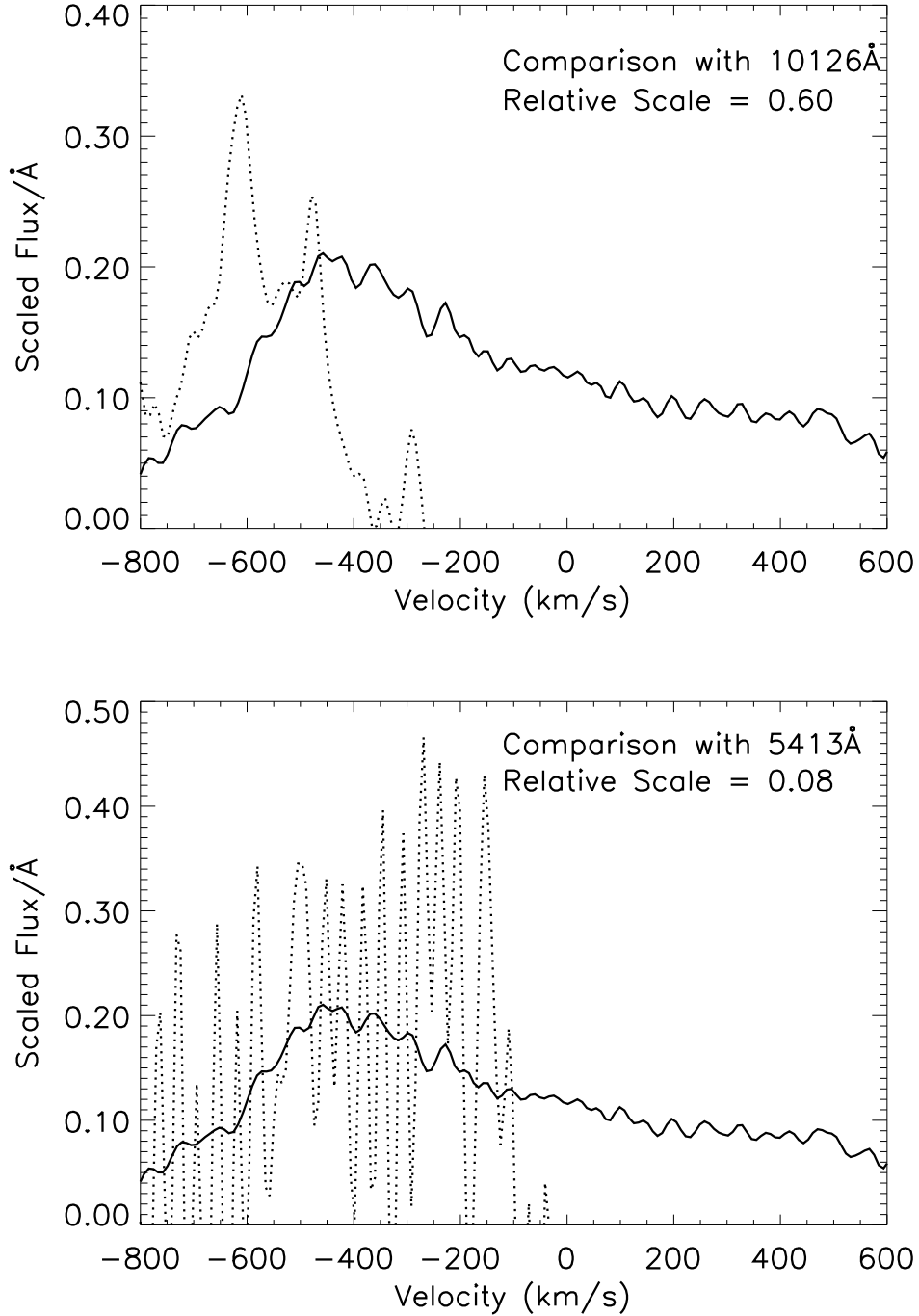


Fig. 7.— A comparison of the observed flux profiles of other He II lines observed on MJD 52813.8 with the profile observed near He II λ 4687 (solid line in both panels). See text for full description. Top panel: a comparison with the observed flux near He II λ 10126 (dotted line). Bottom panel: a comparison with the observed flux near He II λ 5413 (dotted line).

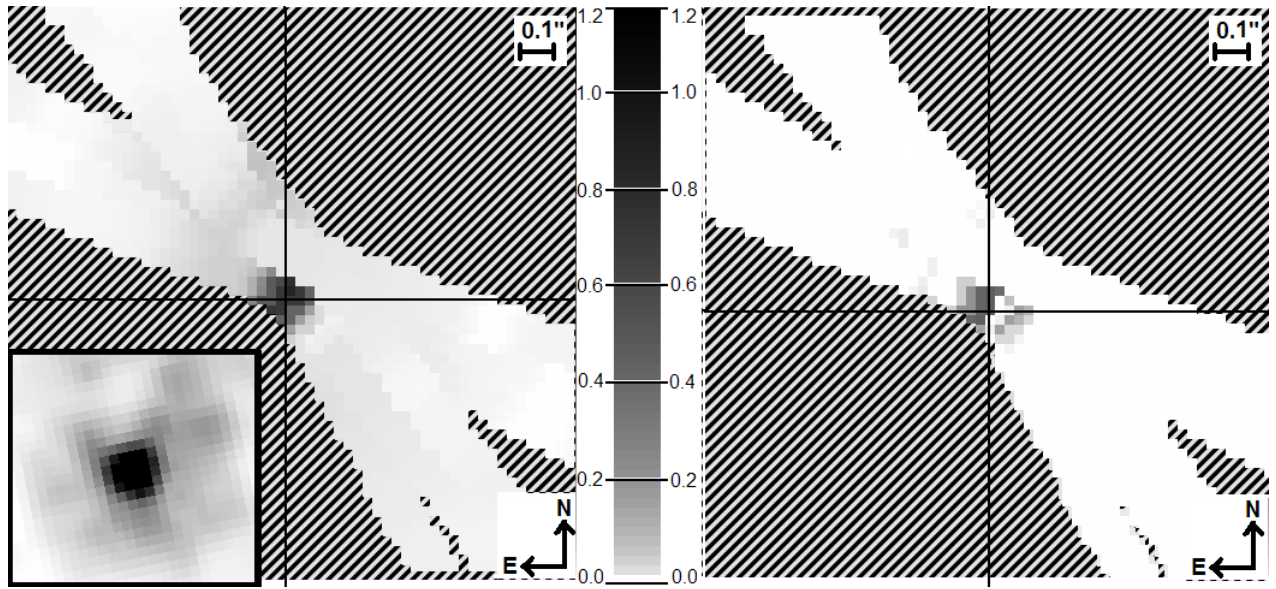


Fig. 8.— These maps are made from seven separate STIS slits observed between MJD 52764 (2003.34) and MJD 52813 (2003.47). The diagonally hashed area is not covered by any slit during that time period. The relative flux scale is given in the center. The right panel is a map of the 4680 Å emission, the left panel is a map of the 4743 Å continuum, and the insert at lower left is an HST ACS/HRC image at the same scale and orientation taken with the F330W filter on MJD 52896. The cross-hairs in both panels mark the location of the central star. The slight asymmetry with respect to the position of the central star in the map of 4680 Å emission is a product of the pixel interpolation method and is not present in the raw STIS data.

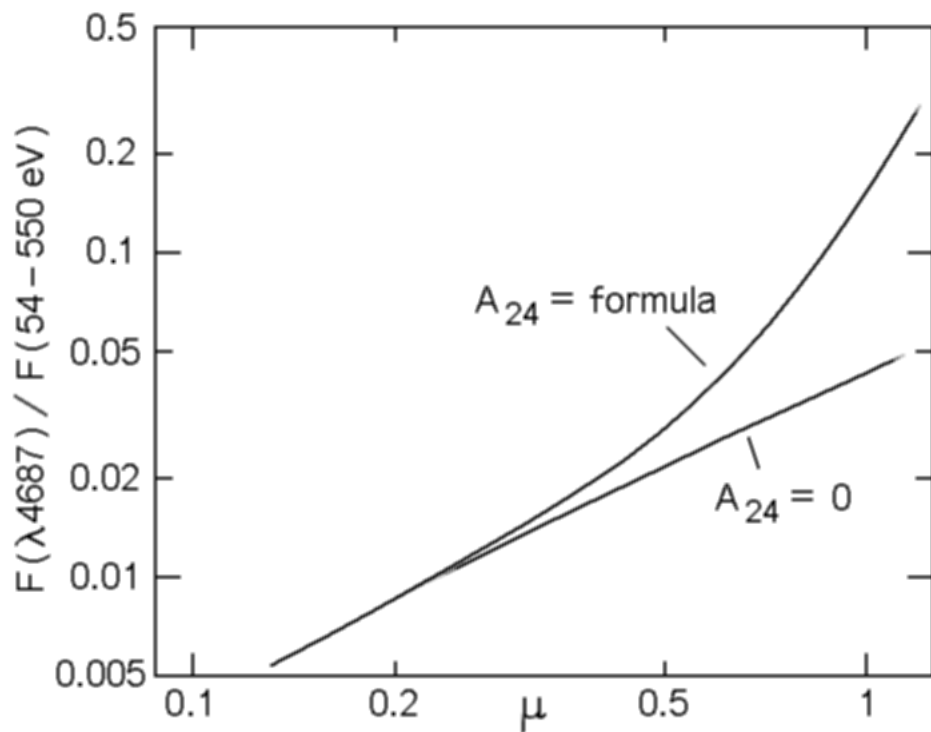


Fig. 9.— The ratio of He II $\lambda 4687$ to the input soft X-ray flux as a function of μ . The upper curve includes excitation by Lyman α and the lower curve omits that factor.

Table 1. Measured Flux and Equivalent Width of the 4680Å Feature

MJD	Year	S/N ^c	Continuum Flux ^a (erg cm ⁻² s ⁻¹) $\times 10^{-11}$	Line Flux ^b (erg cm ⁻² s ⁻¹) $\times 10^{-12}$	Line EW ^b (Å)
50891.4	1998.21	79	2.51 \pm 0.03	-0.12 \pm 0.45	-0.09 \pm 0.18
51230.5	1999.14	126	4.31 \pm 0.03	-0.47 \pm 0.48	-0.21 \pm 0.11
51623.8	2000.22	140	6.00 \pm 0.04	-0.10 \pm 0.61	-0.12 \pm 0.10
52016.8	2001.29	109	5.16 \pm 0.05	-0.63 \pm 0.67	-0.23 \pm 0.13
52294.0	2002.05	110	5.03 \pm 0.05	-0.26 \pm 0.64	-0.10 \pm 0.13
52459.5	2002.51	130	4.90 \pm 0.04	-0.29 \pm 0.53	-0.11 \pm 0.11
52683.1	2003.12	121	4.73 \pm 0.04	0.82 \pm 0.56	0.33 \pm 0.12
52727.3	2003.24	102	5.03 \pm 0.05	0.67 \pm 0.70	0.25 \pm 0.14
52764.3	2003.34	97	4.48 \pm 0.05	2.20 \pm 0.67	0.93 \pm 0.15
52778.5	2003.38	118	4.86 \pm 0.04	2.22 \pm 0.60	0.87 \pm 0.12
52791.7	2003.42	144	5.20 \pm 0.04	3.35 \pm 0.53	1.23 \pm 0.10
52813.8	2003.47	107	5.88 \pm 0.05	7.38 \pm 0.83	2.38 \pm 0.13
52825.4	2003.51	113	6.05 \pm 0.05	0.25 \pm 0.76	0.08 \pm 0.12
52852.4	2003.58	108	6.17 \pm 0.06	0.06 \pm 0.81	0.02 \pm 0.13
52904.3	2003.72	148	8.31 \pm 0.06	-0.03 \pm 0.79	-0.01 \pm 0.09
52960.6	2003.88	150	9.12 \pm 0.06	-0.03 \pm 0.86	-0.01 \pm 0.09
53071.2	2004.18	140	8.92 \pm 0.06	-0.28 \pm 0.90	-0.06 \pm 0.10

^aThe estimated continuum flux from 4675Å to 4694Å based on the measured flux between 4742.5Å and 4746.5Å (see text).

^bFluxes and equivalent widths are expressed relative to the continuum with values greater than zero denoting excess flux above the continuum.

^cAs computed from the ratio of the average flux per Å and the standard deviation of the flux in the continuum over the range from 4742.5Å to 4746.5Å. See Appendix B.

Table 2. Predicted He II Line Fluxes

Wavelength (Å in Vacuum)	Relative Strength ^a	Predicted Flux ^e (erg cm ⁻² s ⁻¹) $\times 10^{-13}$	Detection Limit ^b (erg cm ⁻² s ⁻¹) $\times 10^{-13}$	Notes
1640	8.150	601.	5.70	High extinction ^d
2386	0.104	10.3	6.52	High extinction ^c
2512	0.193	14.2	5.81	High extinction ^c
2734	0.257	19.0	5.87	High extinction ^c
3204	0.469	34.6	6.02	Confusion with other features ^c
3797	0.003	0.221	9.26	Blend with Balmer line
3925	0.008	0.590	6.96	
4101	0.015	1.11	8.75	Blend with Balmer line
4339	0.026	1.92	6.90	Blend with Balmer line
4543	0.036	2.66	7.18	
4687	1.000	73.8	7.69	
4861	0.053	3.91	7.82	Blend with Balmer H β
5413	0.080	5.90	16.0	
6562	0.134	9.88	15.7	Blend with Balmer H α
10126	0.237	17.5	19.8	High CCD noise

^aRelative to F(He II 4687Å)=1.0. Taken from Osterbrock (1989) for T=40,000 K and $4\pi j_{\lambda 4686}/N_{He}++N_e = 3.48 \times 10^{-25}$ (erg cm⁻² s⁻¹).

^bMinimum detectable line flux in the STIS/CCD data at that wavelength given the detector and photon noise assuming that the line has a Doppler width of about 600 km s⁻¹. (See Appendix B)

^cHeavy line blanketing made it difficult to sample the continuum so the STIS Spectroscopic Exposure Time Calculator (<http://apt.stsci.edu/webetc/stis/stisspec.jsp>) was used to compute the expected S/N for the spectrum.

^dThe detection limit is estimated for our E140M MAMA observation using the STIS Spectroscopic Exposure time calculator. If the MAMA data were binned to the same resolution as the CCD data, the detection limit would be a factor of $\sqrt{2}$ smaller.

^eCalculated without considering extinction effects.

Table 3. Relative Noise Levels and Constraints on He II Emission in STIS Data Before 2003.00 and After 2003.50

MJD ^a	Year	σ ^b	E.W. (mÅ) ^c
50891	1998.21	0.0079	+24 ± 36
51230	1999.14	0.0075	+1 ± 34
51624	2000.22	0.0092	-50 ± 42
52017	2001.29	0.0088	-61 ± 40
52294	2002.05	0.0073	+14 ± 34
52460	2002.51	0.0084	+33 ± 38
52683 ^d	2003.12	0.0098	+182 ± 45
52825	2003.51	0.0073	-37 ± 36
52852	2003.58	0.0061	+44 ± 29
52904	2003.72	0.0078	+27 ± 36
52961	2003.88	0.0077	+43 ± 35
53071	2004.18	0.0064	+18 ± 29
(av) ^e	—	0.0029	-11 ± 14

^aModified Julian Day Number

^bRelative r.m.s. noise in a 0.276 Å sample,
see text

^cFormal emission equivalent width in least-squares fit

^dHe II emission was clearly present at 2003.12; included for comparison only, see text

^eResults in spectrum averaged over all these data sets except 2003.12, see text